Murine classical monocyte subsets display distinct functions and fates

Sébastien Trzebanski[1], Jung-Seok Kim[1], Niss Larossi[1], Daliya Kancheva[2], Jonathan Bastos[2], Montaser Haddad[1], Dan Aizik[1], Jarmila Kralova[1], Mor Gross-Vered[1], Sigalit Boura-Halfon[1], Tsvee Lapidot[1], Ronen Alon[1], Kiavash Movahedi[2] and Steffen Jung[1 †]

[1]Department of Immunology and Regenerative Biology, Weizmann Institute of Science, Rehovot 76100, Israel.
[2]Laboratory for Molecular and Cellular Therapy, Vrije Universiteit Brussel, Brussels Belgium

[†] Corresponding author e-mail: s.jung@weizmann.ac.il (S.J.)

Keywords: monocytes, NeuMo, DCMo, macrophages,

Abstract

Monocytes are short-lived myeloid immune cells that arise from adult haematopoiesis and circulate in the blood after maturation. Monocytes comprise two main subsets, that are in mice defined as classical Ly6C^{high} and non-classical Ly6C^{low} cells (CM, NCM). Recent transcriptomic analyses suggest that CM themselves are heterogeneous. Here, we report surface markers that allow segregation of murine neutrophil-like and DC-like CM (NeuMo, DCMo) in the BM and blood. Functional characterization, including fate definition following adoptive cell transfer, established that NeuMo and DCMo can give equal rise to homeostatic CM progeny, such as NCM and gut macrophages. Fates differed, however, in selected other tissues, such as the lungs and brain meninges. Collectively, we provide comprehensive evidence for the existence of two functionally distinct CM subsets in the mouse, which differentially contribute to peripheral tissue macrophage populations, indicative of impact of monocyte ontogeny on *in situ* differentiation.

Introduction

Monocytes are circulating short-lived myeloid immune cells that promote inflammation and serve as precursors of tissue-resident macrophages [1]. Monocytes arise from committed progenitors in the bone marrow (BM) [2,3] and are released into the blood stream upon maturation. Under homeostatic conditions, monocytes replenish selected tissue macrophage compartments to various extent. This includes barrier organs, such as the gut and skin, but also tissues that experience mechanical stress, like the heart [4].

In humans, mice, and other mammals, two main subsets of blood monocytes have been identified [5–8]. Murine monocytes have been subdivided into Ly6C^{high} CCR2^{+} 'inflammatory' or classical monocytes (CM) and Ly6C^{low} CCR2^{-} 'patrolling' or non-classical monocytes (NCM) [6,7,9]. Apart from distinct surface marker profiles and transcriptomes [10], monocyte subsets differ, as suggested by their names, also in function. CM are generated in the BM and have short circulation half-lives of about a day in both mice and humans [11,12]. CM are major contributors to tissue resident macrophage populations, both in homeostasis and inflammation [1,11,13]. Within tissues, CM give rise to monocyte-derived macrophages (MoMF) and, potentially, CD209a^{+} monocyte-derived dendritic cells (MoDC) [14–17]. NCM, on the other hand, arise in the circulation from CM in a Notch-dependent manner [18–20]. NCM patrol the wall of blood vessels [9,21], depend on Cx$_3$cr1 for survival [22], are longer-lived than CM [11,12], and can be considered vasculature-resident macrophages. Further, NCM have also been reported to give rise to tissue-resident cells [23–25], although their precursor function is less well established.

Recent studies have revealed further complexity in BM monopoiesis [26,27]. Specifically, adoptive cell transfer and lineage tracing studies suggest a developmental bifurcation that gives rise to two types of CM exhibiting neutrophil or dendritic cell (DC) features, respectively. Neutrophil-like monocytes (NeuMo) were proposed to arise from granulocyte and macrophage progenitors (GMP) and are defined by transcripts encoding neutrophil granule proteins, such as elastase (*Elane)*, myeloperoxidase (*Mpo*), and chitinase-like protein 3 (*Chil3)* [26,27]. DC-like monocytes (DCMo), on the other hand, are thought to emerge from monocyte and DC precursors (MDP) and their transcriptome was reported to be enriched for transcripts related to MHC-II expression and encoding classical DC markers, such as *Cd209a* [26,27]. Interestingly, and suggesting discrete functional roles of these CM subsets, distinct challenges seem to result in selective expansion of NeuMo and DCMo populations [26]. However, CM heterogeneity remains largely defined by transcriptomics and functional contributions and fates of NeuMo and DCMo upon their recruitment into tissues remain to be elucidated.

Here, we report surface markers that allow the discrimination of murine NeuMo and DCMo as CD177$^+$ and CD319$^+$ CM, and enabled us to perform a comprehensive analysis of *in vitro* and *in vivo* features of these cells. Corroborating earlier work, mice challenged with different microbial stimuli exhibited distinct NeuMo and DCMo dynamics. Further, classical *in vitro* assays for neutrophil-related activities established unique functional potential of NeuMo and DCMo. Finally, competitive adoptive transfers of the two CM populations into macrophage-depleted animals revealed overlapping and distinct contributions of NeuMo and DCMo to peripheral tissue resident macrophages, including the gut, lung, and meninges.

Results

Identification of surface markers discriminating murine classical monocyte subsets

Emerging evidence suggests discrete neutrophil- and DC-like subpopulations among CM [8,26,27]. However, except for a recent study [28], CM heterogeneity has not been established beyond mere transcriptomics, although the identification of surface markers is crucial to investigate functional aspects of these CM subsets in physiological setting. In search of such markers, we therefore decided to perform a comprehensive CITE-seq screen on whole BM isolated from C57BL/6 wild type (wt) animals (**Fig 1A**). All myeloid immune subsets and their precursors were well represented in our data set (**Fig 1B, Suppl Fig 1A,B,C**). Anti-Ly6C and -CD115 TotalSeq antibodies reliably identified *Csf1r*$^+$ and *Fcgr3*$^+$ monocytes and their precursors (**Fig 1C**). Focusing on mature monocytes and nearby clustering classical DC (cDC), we identified a small cluster of Ly6C$^+$ CD115$^+$ *Fcgr3*$^+$ monocytes devoid of the CM marker CD62L (encoded by *Sell*) [6,7] (**Fig 1D**). Differential expression analysis between the CD62L$^+$ and the CD62L$^-$ CM clusters, highlighted enriched expression of neutrophil related genes, such as *Chil3*, *Mmp8,* and *Slpi* in CD62L$^+$ CM, while MHC-II transcripts were upregulated in the CD62L$^-$ subset (**Fig 1D,E**). Interestingly, despite their high expression of MHC-II transcripts, these cells were otherwise transcriptionally and phenotypically distinct from cDC, suggesting that they might be DC-like monocytes (**Fig 1F**).

Closer examination of the list of differentially expressed genes (DEG) between the CD62L$^+$ and CD62L$^-$ monocyte clusters revealed *Slamf7* (encoding CD319) restricted to CD62L$^-$ cells (**Fig 1D,E**). Further, *Cd177* was seemingly ubiquitously expressed in CD62L$^+$ cells. Of note, *Cd177* was also among the top 10 DEG reported for NeuMo [27] (**Fig 1D, Suppl Fig 1G**). Indeed, a combined staining for CD319 (clone 4G2) and CD177 (clone Y127) provided sufficient segregation of two Ly6C^{high} CM subsets via flow cytometry (**Fig 1G**). Importantly, proportions of CD177$^+$ and CD319$^+$ CM were in line with previous estimates for the reported steady state NeuMo / DCMo ratio [29]. Moreover, an independent LEGENDscreen approach on total blood cells revealed CD319 to yield sufficient segregation of CM when plotted against CD177 (**Suppl Fig 1D**). Interestingly, among other blood

immune cell subsets, CD177 expression was restricted to neutrophils while CD319 was expressed on cDC and lymphocytes but not neutrophils (**Suppl Fig 1E,F**).

Phenotypic characterization of CD177$^+$ and CD319$^+$ blood CM via flow cytometry confirmed equal levels of Ccr2 on the surface of both cells, as well as lower CD62L expression on CD319$^+$ CM (**Fig 1H**). CD177$^+$ CM displayed a shift for CD88a and Ly6C, while CD319$^+$ CM showed higher expression of MHC-II, the chemokine receptor Cx_3cr1, and the Fc receptor CD64 (**Suppl Fig 1G**). Importantly and underlining the robustness of our finding, differential CD177 and CD319 expression on blood CM could be independently confirmed in another animal facility (**Suppl Fig 1I**). Lastly, CD177$^+$ but not CD319$^+$ blood CM, expressed higher levels of CD157 (BST1), in line with a recent report identifying CD157 and CD88a as neutrophil-like CM markers [28] (**Suppl Fig 1J**).

DC precursors display a number of classical CM surface markers, including CD115 and Ly6C [30]. We therefore probed for a potential contamination of the CD319$^+$ CD11c$^-$ CM gate with CD11c$^+$MHC-II$^-$ pre-cDC by analysis of Flt3 expression and intracellular staining for the cDC lineage-determining transcription factor (TF) Zbtb46 [31,32] (**Suppl Fig 1K**). Neither Zbtb46 nor Flt3 were found to be expressed by CD319$^+$ CM (**Suppl Fig 1L**).

In summary, we identified CD177 and CD319 as surface markers delineating phenotypically distinct CM subsets.

CD177$^+$ and CD319$^+$ CM are NeuMo and DCMo, respectively

To establish the relation of our new phenotypically identified CM subsets to the NeuMo / DCMo signatures [26,27], we performed a global RNAseq analysis of CD177$^+$ and CD319$^+$ Ly6C^{high} CM, as well as CD177$^-$ CD319$^-$ double negative (DN) Ly6C^{high} CM, sorted to purity from the peripheral blood of *Cx3cr1$^{Gfp/+}$* animals [33] (**Suppl Fig 2A**). We identified 41 genes specifically expressed in CD177$^+$ CM and 67 genes whose expression was enriched in CD319$^+$ CM (**Fig 2A**). This differential gene signature related to that of the putative NeuMo and DCMo clusters observed in the BM via CITE-seq **(Fig 1E)**, with many top genes being shared. Global analysis revealed 141 genes differentially expressed by CD319$^+$ CM, and 108 genes highly expressed in CD177$^+$ CM and DN cells (**Fig 2B**), suggesting that the latter two populations are closely related (**Fig 2C**). Importantly, *Zbtb46* was not detected in either CM subset, corroborating the absence of DC contamination. Comparison of our data to a published NeuMo / DCMo dataset based on bioinformatic predictions [27] revealed a considerable overlap (**Suppl Fig 2B**). This establishes that CD177$^+$ and CD319$^+$ CM represent NeuMo and DCMo, respectively. Furthermore, in line with the bulk RNAseq data, Clec10a and CD209a were also higher expressed on the surface of DCMo compared to CD319$^-$ cells (**Suppl Fig 2C**). Of note, NeuMo and DCMo CM gene clusters could also be

identified in a previously published single-cell dataset of total blood monocytes [10] (**Suppl Fig 2D**).

Confirming their *bona fide* monocyte nature, all CM subsets expressed high levels of *Spi1* encoding the pioneering transcription factor (TF) PU.1, and *Klf4*, as well as the lineage markers *Cx3cr1* and *Csf1r* (encoding CD115) (**Fig 2D**). CD319$^-$ NeuMo displayed high expression of genes encoding neutrophil-related markers, such as *Chil3* and *Mmp8* encoding granule proteins [34,35], as well as the peptidoglycan recognition protein, *Pglyrp1*. Further, NeuMo expressed high *Cebpb* transcript levels, encoding a TF known to be important for CM conversion into NCM [10,36] (**Fig 2D**). DCMo were enriched in transcripts encoding immune-modulatory DC-related molecules, such as *H2-Ab1*, *Btla*, and *Cd40*, as well as the TF *Batf3*, akin to previously described *Cd209a*$^+$ Ly6C^{int} monocytes [10] (**Fig 2D**). Finally, Metascape analysis [37] indicated enrichment in neutrophil and DC modules, such as '*neutrophil degranulation'* and '*negative regulation of immune system process'* in NeuMo and DCMo, respectively (**Fig 2E**).

Taken together, CD177$^+$ NeuMo and CD319$^+$ DCMo displayed distinct transcriptional landscapes, which are in line with previously reported profiles [10,26,27]. Moreover, our data establish that the majority of Ly6C^{high} CM, including CD177$^-$ CD319$^-$ cells, in the blood of healthy C57BL/6 mice kept under hyper-hygienic conditions, comprises cells displaying a NeuMo signature.

CD177$^+$ NeuMo and CD319$^+$ DCMo CM arise in the BM as GMP and MDP progeny, respectively

Goodridge and colleagues proposed that NeuMo and DCMo derive from GMP and MDP, respectively [26]. Accordingly, also CD177$^+$ NeuMo would be expected to arise mostly from GMP, whereas CD319$^+$ DCMo should be progeny of MDP. As previously reported [13], *Ms4a3^{Cre}:R26$^{LSL-TdTom}$* animals, which allow the mapping of the fate of GMP, harbor a small percentage of unlabeled blood CM (**Fig 2F**). Interestingly, these unlabeled cells showed robust, albeit not exclusive, expression of CD319, as well as higher Cx$_3$cr1 expression levels, akin to blood DCMo (**Fig 1F,I, Suppl Fig 1F**).

To further explore the link between ontogeny and NeuMo and DCMo, we next took advantage of *Ms4a3^{Cre}:R26$^{LSL-TdTomato}$:Cx3cr1^{gfp}* double reporter mice, in which GMP- and MDP- progeny can be discriminated according to its reporter gene expression. We isolated TdTom$^+$ GFP$^+$ and TdTom$^-$ GFP$^+$ CM from BM of these animals, further enriched for lack of CD11c and MHC-II expression to exclude cDC and their precursors (**Suppl Fig 2E**), and subjected them to bulk RNAseq analysis. In line with the proposed developmental scheme [13,26], GFP$^+$ BM monocytes expressed higher levels of DC-related transcripts, such as *H2-Ab1* and *Cd209a*, whereas TdTom$^+$ GFP$^+$ BM monocytes displayed a neutrophil-like gene

expression signature, including *Chil3* and *Elane* (**Fig 2G,H, Suppl Fig 2F**). Further, MDP- and GMP-derived cells exclusively overlapped with DCMo and NeuMo transcriptomes, respectively (**Suppl Fig 2G**). Of note, *Cd177* and *Slamf7* were lowly expressed in BM monocytes (**Fig 2H**). This might be due to the generous CD11b sorting gate (**Suppl Fig 2E**), most likely including immature CD11b^{int} transitional pre-monocytes [38]. Further, this would explain the expression of *Flt3* and neutrophil granule proteins, such as *Mpo* and *Ngp*, which was absent from blood monocytes (**Fig 2G**).

In conclusion, we corroborate the earlier notion that BM monopoiesis is bifurcated and includes a GMP - NeuMo and a MDP - DCMo axis.

NeuMo and DCMo prevalence following exposure to microbial stimuli and IFNγ

The CM compartment dynamically responds to challenges including exercise, metabolic alterations, and pathogen encounter [39,40]. Under conditions of parasitic and bacterial inflammation associated with IFNγ exposure, CM have been shown to upregulate expression of the stem cell marker Sca1 (Ly6A) and concomitantly downmodulate the monocyte/macrophage lineage marker Cx$_3$cr1 [41,42].

GMP-derived NeuMo and MDP-derived DCMo were reported to differentially expand in animals challenged with LPS and CpG [26]. In line with these findings, exposure of wt C57BL/6 animals to LPS (2.5 ug/g, i.p. or i.v.) resulted by day 1 in an increase in CD177$^+$ cells while DCMo remained proportionally unaffected (**Fig 3A,B, Suppl Fig 3B**). Surprisingly, Cx$_3$cr1 surface expression was selectively lost on NeuMo, whereas DCMo retained normal Cx$_3$cr1 levels (**Fig 3C**). Conversely, DCMo and DN CM exclusively upregulated Sca1 (**Fig 3C**). Furthermore, DCMo and DN CM showed induction of DCMo markers, including CD64, CD11c, and CD209a (**Suppl Fig 3C**). Interestingly, these changes in Cx$_3$cr1 and Sca1 expression were also found to be correlated on Ly6C$^+$ GMP and MDP in the BM (**Suppl Fig 3D,E,F**).

The TLR9 agonist CpG was reported to expand DC-like monocytes [26]. Accordingly, administration of CpG + DOTAP (5 ug/mouse and 25 ug/mouse, respectively) increased the representation of DCMo within the blood Ly6C$^+$ CM gate at the expense of NeuMo (**Fig 3D,E, Suppl Fig 3G**). As opposed to the LPS regimen, the CM subsets were equally affected following this challenge. Specifically, Sca1 was strongly upregulated on all CM subsets while Cx$_3$cr1 expression remained unaltered (**Fig 3F**). In contrast to LPS-treated mice, and testifying monocyte plasticity, NeuMo upregulated DCMo markers CD64, CD11c, and CD209a following CpG exposure (**Suppl Fig 3H**). Again, also BM precursors showed distinct surface phenotypes after CpG-activation (**Suppl Fig 3I,J,K**).

Infection-associated IFNγ prompts the emergence of Sca1$^+$ monocytes [41,42]. Indeed, like the CpG challenge, DCMo were significantly expanded in the CM gate of mice given a one-time injection of 5 ug recombinant IFNγ (rIFNγ), at the expense of CD177$^+$ NeuMo (**Fig 3G,H, Suppl Fig 3L**). Cx3cr1 expression did not change significantly on any of the subsets, while Sca-1 was significantly higher expressed on DCMo (**Fig 3I**). CD319$^-$ CM modestly upregulated MHC-II, whereas DCMo expressed high levels of both MHC-II and CD11c (**Suppl Fig 3M**). Transcriptome analysis of sorted Sca1$^+$ and Sca1$^-$ CM retrieved from blood of animals that underwent repetitive rIFNγ challenges (**Suppl Fig 3N**) revealed that Sca-1$^+$ CM expressed *Slamf7* (encoding CD319), whereas Sca-1$^-$ CM displayed higher expression of *Cd177* and *Fpr2* (**Suppl Fig 3O,P,Q**). This suggests that distinct NeuMo and DCMo signatures are retained, at least on the transcriptional level, following challenges.

Collectively, and as previously described for GMP- and MDP-derived BM monocytes [26], CD177$^+$ NeuMo and CD319$^+$ DCMo differentially expand following exposure to microbial stimuli, likely as a result of altered monopoiesis.

NeuMo but not DCMo display distinct neutrophil-like functions *in vitro*

Neutrophils are first-responders at sites of sterile and non-sterile injury, where they function as phagocytes and neutralize extracellular pathogens [43–45]. To investigate if NeuMo share, beyond their transcriptomic overlap, functional neutrophil hallmarks, we performed a series of *in vitro* assays (**Fig 4A**).

N-formylpeptides are cleavage products of bacterial and mitochondrial proteins that act as potent neutrophil chemoattractants [46]. The N-formylpeptide receptor 2 (Fpr2) was robustly and differentially expressed in NeuMo (**Fig 4B**). To test for its activity, we magnetically enriched CD115$^+$ BM monocytes and subjected them to a migration assay towards 100 nM fMLP or carrier control (**Fig 4C, Suppl. Fig 4A,B**). Analysis of migration towards fMLP-supplied medium revealed that CD177$^+$ NeuMo displayed a 10-fold enrichment compared to the control condition, while CD319$^+$ DCMo did not migrate at all in this assay (**Fig 4C**).

A hallmark of neutrophil activation is the formation of extracellular traps (ET) that are linked to granule protein expression, including MPO, as well as histone citrunillation and deamination [43]. NeuMo, but not DCMo, expressed one of the key factors required for chromatin de-condensation, the protein-arginine deiminase type-4 (Padi4) as well as high levels of intracellular MPO [47] (**Fig 4D**). To test whether Padi4 endows NeuMo with potential to form ET, CD177$^+$ NeuMo, CD319$^+$ DCMo, and neutrophils were sorted to purity and activated by PMA for six hours. Staining for DNA, MPO, and citrullinated H3 revealed a

significantly higher propensity of triple-positive events in NeuMo, compared to DCMo (**Fig 4E**). This is in line with earlier reports of ET formation by human monocytes [48].

To compare the phagocytic potential of NeuMo and DCMo, CD177$^+$ and CD319$^+$ BM monocytes were sorted to purity and incubated with GFP-expressing *Salmonella typhimurii* for two hours. Flow-cytometric analysis revealed that NeuMo showed a superior capability to internalize bacteria (**Fig. 4F, Suppl Fig 4C**). However, also DCMo showed robust phagocytosis activity in this assay, in line with their monocyte nature.

Taken together, these *in vitro* assays suggest that, beyond their transcriptomic disparities, NeuMo also display functional activities that differentiate them from DCMo. This includes classical neutrophil activities, such as attraction by bacterial peptides, ET formation, and phagocytosis.

NeuMo and DCMo give rise to NCM and intestinal macrophages

A main homeostatic function of monocytes is to maintain selected longer-lived tissue-resident macrophage compartments, including mucosal tissues [1,49,50]. To investigate prospective fates of CD177$^+$ NeuMo and CD319$^+$ DCMo, we isolated the two CM subsets from reporter animals that endow them with a discrete label, i.e. *Cx3cr1^{gfp}*, *Cx3cr1^{Cre}:R26$^{LSL-TdTomato}$* and *Ms4a3^{Cre}:R26$^{LSL-TdTomato}$* mice [11,13,33], and performed adoptive transfer experiments. To free niches for engraftment [51], we took advantage of irradiation chimeras generated with *Cx3cr1^{DTR}* BM as recipients. Specifically, diphtheria toxin (DTx) treatment of these animals results in depletion of monocytes and Cx$_3$cr1$^+$ macrophage populations [52,53].

Equal amounts of NeuMo and DCMo (2 x 10^5) were co-transferred into DTx-treated *Cx3cr1^{DTR}* chimeras 8-10 weeks after irradiation and BM transfer (BMT) (**Fig 5A**). Depletion of blood monocytes, including CM and NCM, by DTx was confirmed by flow cytometry (**Fig 5B**). Blood analysis of some recipient animals on day 1 after transfer, revealed circulating engrafted TdTom$^+$ NeuMo and GFP$^+$ DCMo, at roughly equal numbers (**Fig 5C**). In line with earlier reports and indicating differentiation towards NCM [18], both cell types had begun to downregulate Ly6C (**Fig 5C**). When bled on day 3 after transfer, the analysis revealed that both NeuMo and DCMo cells had converted into Ly6C^{low} NCM while maintaining the ratios (**Fig 5D**). Surface marker profiling revealed similar expression of the integrin CD11c among NeuMo- and DCMo-derived NCM (**Fig 5E**). However, DCMo-NCM displayed significantly higher expression of PDL1, a recently reported NCM marker [54] (**Fig 5E**). Conversely, the classical monocyte markers CD115 and CD11b, were higher expressed on NeuMo-derived NCM, albeit not reaching significance (**Fig 5E**).

On day 12 after transfer, several organs of the recipient mice were harvested to investigate the potential of NeuMo and DCMo to give rise to long-lived tissue resident macrophages [18,51,55]. In both ileum and colon, clones of NeuMo and DCMo-derived

macrophages were found to have clonally expanded [51] (**Fig 5F**). Quantification of graft-derived macrophages by microscopy and flow cytometry revealed equal contributions to both ileal and colonic macrophage compartments (**Fig 5F,G,H**).

Collectively, we show that following engraftment, both NeuMo and DCMo give in a competitive setting rise to NCM and gut macrophages with comparable efficiency [18,51]. Of, note, NeuMo- and DCMo-derived NCM displayed distinct phenotypes, including PDL1 expression. Differential ontogeny could hence have impact on NCM functions.

NeuMo and DCMo fates in the lung

Pulmonary interstitial macrophages (IM) are heterogenous and comprise CD206$^-$ cells and CD206$^+$ IM [56], as well as lung-resident CD16.2$^+$ cells [23]. The latter were considered IM precursors [23], a finding supported by observations from humanized animals [24], though recent data suggest that IM develop from CM through a proliferating intermediate [57].

Engrafted TdTom$^+$ NeuMo- and GFP$^+$ DCMo-derived cells could be readily detected in the recipient lungs by histology and flow cytometric analysis on day 12 (**Fig 6A, B, Suppl Fig 5A**). Importantly, only very few grafted cells were detected in the blood at day 12 (**Suppl Fig 5B**). Interestingly, TdTom$^+$ and GFP$^+$ cells significantly differed with respect to their relative distribution in specific subpopulations in the pulmonary myeloid compartment. Specifically, the majority of grafted cells in the lung had arisen from DCMo (**Fig 6C**). While both NeuMo- and DCMo-derived cells could be found in roughly similar numbers among CD16.2$^+$ precursors, DCMo-derived mature IM vastly outnumbered NeuMo-derived IM (**Fig 6C**). In fact, DCMo-derived IM were, on average, 4-fold enriched over DCMo-derived CD16.2$^+$ precursors, whereas this ratio was around 1 among NeuMo-derived cells (**Fig 6D**). This delayed or absent differentiation into mature IM by NeuMo was further substantiated by higher CD16.2 and lower MHC-II surface expression on NeuMo- compared to DCMo-derived IM (**Fig 6E, Suppl Fig 5C**).

To further study the pulmonary NeuMo and DCMo progeny, we performed bulk RNAseq on engrafted TdTom$^+$ and GFP$^+$ cell retrieved from recipient lungs (**Suppl Fig 5D**). Out of a total number of 220 DEG, 48 genes were preferentially expressed in DCMo-derived cells, while 172 genes displayed higher transcription in NeuMo-derived cells (**Fig 6F, Suppl Fig 5E**). Metascape analysis [37] revealed enrichment in *angiogenesis* and *wound healing* pathways in the NeuMo-derived IM profile (**Suppl Fig 5F**). Conversely, DCMo-derived IM were associated with gene modules regulating the *immune response* and *leukocyte differentiation* (**Suppl Fig 5F**). Interestingly, the transcriptome of NeuMo progeny showed significant overlap with an expression signature reported for Lyve1$^+$MHC-II^{low} lung IM, while DCMo progeny was more akin to Lyve1$^-$MHC-II^{hi} lung IM [58] (**Fig 6G, Suppl Fig 5G,H**). Moreover, compared to NeuMo-IM, cells derived from DCMo induced twice higher

expression of Mafb, a TF recently suggested to be required for CM differentiation into lung IM [57] (**Fig 6H**). Conversely, expression of *Maf,* encoding c-MAf which was proposed to imprint CD206$^+$ IM identity [57], did not show significant distinct expression among NeuMo- and DCMo-derived IM (**Fig 6H**).

To directly link this dichotomy to ontogeny, we next performed a competitive adoptive transfer of GMP- and MDP-derived monocytes isolated from BM of *Ms4a3^{Cre}:R26$^{LSL-TdTomato}$:Cx3cr1^{gfp}* mice (**Fig 6I**). Indeed, MDP-derived GFP$^+$ monocytes also preferentially gave rise to IM over GMP-derived TdTom$^+$GFP$^+$ CM (**Fig 6J,K**). Furthermore, CD16.2 expression was higher on GMP-derived CD206$^+$ IM, in line with the phenotype of NeuMo-derived IM (**Fig 6L**). Interestingly, and in line with transcriptome data, GMP-derived IM expressed higher surface levels of Lyve1. However, we observed no differential MHC-II expression on either graft-derived IM population.

In conclusion, using a competitive adoptive transfer approach, we establish that NeuMo and DCMo have distinct differentiation trajectories upon their seeding of the lung. Furthermore, these fates are determined by ontogeny.

NeuMo but not DCMo, give rise to meningeal dura mater macrophages

The macrophage compartment of the central nervous system (CNS) comprises parenchymal microglia, meningeal macrophages in dura mater and leptomeninges, as well as macrophages in the perivascular space and choroid plexus [59,60].

To probe the ability of NeuMo and DCMo to replenish CNS macrophage niches, we analyzed the brains of DTx-treated *Cx3cr1^{DTR}* chimeras on day 12 and 21 after engraftment (**Fig 5A**). The brain parenchyma of the recipient mice was devoid of graft-derived labelled cells, in line with DTx insensitivity of this compartment due to the limited replacement of microglia by DTR transgenic cells in the BM chimeras [61] (**Suppl Fig 6A**). In contrast, meningeal macrophages of the *Cx3cr1^{DTR}* chimeras were partially depleted by the DTx regimen (**Suppl Fig 6B**). Nevertheless, no labelled cells were detected in the leptomeninges of the recipient mice (**Suppl Fig 6B**). Surprisingly, however, we observed an efficient repopulation of macrophages in the dura mater, albeit exclusively by TdTom$^+$ NeuMo (**Fig 7A,B**). Specifically, cells concentrated along the sagittal sinus, but could also be found in more distant areas (**Fig 7A, Suppl Fig 6C**). Engraftment was sustained, since TdTom$^+$ cells were still abundantly present 3 weeks after transfer, suggesting *in situ* proliferation of the graft (**Fig 7B**). Results were confirmed in independent transfer experiments in which we switched the labels, engrafting TdTom$^+$ DCMo and GFP$^+$ NeuMo (**Suppl Fig 6D**). By day 12, NeuMo-derived cells had acquired low levels of CD206 expression, a hallmark of dura mater macrophages [60] (**Fig 7C**). However, surface MHC II expression and higher levels of CD206 were only detected at day 21, suggesting *in situ* maturation of the cells (**Fig 7D**).

To investigate the underlying mechanism of the selective recruitment of NeuMo but not DCMo to the dura mater, we turned to the list of differentially expressed trafficking molecules. Specifically, we noted high level of expression of *Sell*, encoding for CD62L, by NeuMo (and DN CM), as compared to DCMo, both on the transcriptional and protein level (**Fig 7E**), as also shown via CITE-seq for BM subsets (**Fig 1D**). To probe for a functional relevance of CD62L for the dura mater seeding by CM, we transferred labelled NeuMo into recipient mice which were i.v. treated on two consecutive days with αCD62L antibody (100 ug / mouse) or isotype control (**Fig 7F**). Unimpaired seeding of the colon by grafted cells at 12 days excluded cytotoxicity of the treatment (**Fig 7F, Suppl Fig 6E**). Analysis of the dura mater of the recipients after transfer revealed that αCD62L blockade led to a decrease of $TdTom^+$ dura mater macrophages, compared to control mice (**Fig 7F**).

In conclusion, our data establish differential homing potential of the two CM subpopulations, as NeuMo but not DCMo, are able to repopulate an experimentally depleted dura mater macrophage niche and suggest that the differential seeding is related to NeuMo expression of CD62L.

Discussion

Here, we report the identification of two surface markers, CD177 and CD319, that delineate phenotypically and functionally distinct classical monocyte subsets in the mouse under steady state and challenge, critically extending recent pioneering reports of BM monocyte and CM heterogeneity [26,27]. Furthermore, we establish shared and differential *in vivo* fates of these cells in selected tissues using adoptive transfer experiments into macrophage-depleted animals.

Monocyte subsets were first identified in human blood [5], and the subsequent definition of their murine correlates in *Cx3cr1*^{Gfp} reporter mice [6,7,33] paved the way for functional studies of these cells in organismal context. Specifically, Geissmann and colleagues showed that the murine $Ly6C^{low}$ $CCR2^-$ monocytes monitor blood vessel walls [9]. $Ly6C^{high}$ $CCR2^+$ 'inflammatory' monocytes, on the other hand, perform classical monocyte functions, including, alongside neutrophils, the recruitment to sites of acute inflammation to promote and resolve inflammation. Unlike ephemeral neutrophils, CM can also give rise to long-lived macrophages at sites of injury [4] and progressively replenish selected tissue macrophage compartments in absence of overt inflammation, replacing embryo-derived macrophages with their progeny [51,62]. Progressive exchange of YS-derived tissue macrophages could have long-term impact on the physiological state of tissues during aging. Of note, CM are as HSC progeny, unlike YS-derived macrophages, targets of somatic mutations associated with age-related clonal hematopoiesis (CH). Emerging evidence

indicates that CH-afflicted monocyte-derived macrophages (MoMF) can contribute to cardiovascular and CNS pathologies [63] (*Kim et al, submitted*).

Recent studies revealed transcriptomics-based evidence for CM heterogeneity with neutrophil and DC-like signatures [26,27]. We report here surface markers that discriminate these proposed NeuMo and DCMo among murine Ly6C$^+$ BM and blood CM. We show that, in steady state, the vast majority of murine CM display a NeuMo signature, including CD177$^+$ NeuMo, but also abundant CD177$^-$ CD319$^-$ (DN) CM. Notably, however, we analyzed mice kept under hyper-hygienic special pathogen free (SPF) conditions. NeuMo / DCMo ratios might differ in outbred animals roaming in the wild, given that the relative abundance of the subsets is influenced by the environmental factors.

We define the GPI-linked cell surface glycoprotein CD177 as a NeuMo marker [64]. A recent study revealed NeuMo based on their Ym1 (*Chil3*) expression using a reporter system, as well as surface expression of CD157 (BST1) and CD88a [28]. These data are in line with our finding, as CD177$^+$ NeuMo but not CD319$^+$ DCMo expressed these proteins on their surface. Furthermore, Ym1 reporter-negative CM in the Ikeda *et al* study had higher surface expression of Cx$_3$cr1 compared to Ym1$^+$ CM [28], corroborating the notion that these cells are DCMo and NeuMo as defined in this study, respectively.

We define the SLAM family member 7 (CD319) as a marker for DCMo. Notably, the discrimination of DCMo and DC, including their precursors, remains a formidable challenge. Specifically, these cell types share many surface markers, likely as a result of their common MDP ancestry [2,26,30]. In line with this notion, a Flt3$^+$ BM monocyte subset with antigen-presenting properties has recently been described [65], although this study did not use CD11c as a discriminator between *bona fide* CM and DC. The DCMo we report, do not express Flt3 and we propose that this marker might be uniquely expressed in the DC lineage among mature immune cells. Importantly, the definition of CM as CD11c$^-$ cells [10] removed a considerable contamination of Ly6C$^+$Zbtb46$^+$Flt3$^+$ cells, presumably cDC2 precursors, from the blood CM gate in this study. Crucially, the lineage-defining Zbtb46 TF was not detected in deep sequencing of Ly6C^{high} CD319$^+$ CD11c$^-$ DCMo. Thus, DCMo, as defined in this study, are *bona fide* monocytes and not DC. Moreover, among CM, Clec10a and CD209a can serve as additional DCMo markers.

We confirmed neutrophil and DC gene modules to be differentially expressed in blood NeuMo and DCMo, respectively. Classical neutrophil and DC markers such as *Padi4*, *Fpr2*, and *Chil3* or *H2-Ab1, Cd74,* and *Cd209a* were robustly expressed. Of note, the TF *Cebpb* was differentially expressed in NeuMo while *Batf3* was exclusive to DCMo. Importantly, *Cebpb*$^{-/-}$ CM were shown to express higher levels of *Batf3*, *H2-Ab1*, and *Cd209a* [10]. Further, C/EBPβ was found to be indispensable for the emergence of atypical neutrophil-like monocytes in a model of pulmonary fibrosis [66]. Altogether, this suggests a pioneering

role for CEBPβ in repressing DC-like features in most CM. Interestingly, DCMo also displayed slightly higher expression levels of *Spi1*. This is reminiscent of the earlier notion that higher PU.1 expression might lead to the emergence of CD209a$^+$ MoDC [14].

Importantly, while DCMo share transcriptional similarities with previously described CD209a$^+$ Ly6C^{int} monocytes [10], the cells analyzed in this study were defined and sorted as Ly6C^{high} cells in steady-state conditions. Furthermore, CD319$^-$ CM, but not CD319$^+$ DCMo, displayed higher levels of the TF C/EBPβ shown to be crucial for the conversion of CM to NCM via the Ly6C^{int} monocyte [10]. The relationship of CD319$^+$ Ly6C^{high} CM and CD209a$^+$ Ly6C^{int} cells warrants further scrutiny.

Yáñez *et al.* demonstrated through adoptive cell transfers that NeuMo and DCMo originate from GMP and MDP, respectively [26]. In line with this notion, NeuMo were shown to originate from pro-neutrophils 1 (proNeu1) downstream of GMP in inflammatory conditions [28]. Using *Ms4a3^{Cre}:R26$^{LSL\text{-}tdTomato}$* mice, an established GMP fate mapping model [13] , we could corroborate this scheme. In line with the transcriptomes of NeuMo and CD177$^-$CD319$^-$ CM, more than 95% of blood CM were labeled in the *Ms4a3^{Cre}:R26$^{LSL\text{-}TdTomato}$* mouse corroborating the notion that most CM constitute GMP-derived NeuMo. Conversely, a small fraction of unlabeled CM of the reporter animals expressed higher levels of CD319 and Cx$_3$cr1, suggesting that most DCMo originate from a Ms4a3 independent progenitor, most likely MDP [26,27]. However, it should be noted that GMP-derived CM also comprised DCMo, hinting at an even more intricate bifurcation on the level of the GMP. Importantly, sequencing of Ms4a3^{Cre} tagged and non-tagged BM CM confirmed differential expression of neutrophil and DC genes, respectively, in line with blood NeuMo and DCMo. The exact ontogeny of these CM subsets remains to be investigated.

Based on phenotypic and transcriptional features, the majority of CM in adult C57BL/6 mice kept under hyper-hygienic conditions consists of NeuMo. Following challenges, however, including CpG and IFNγ treatment, DCMo become dominant. A recent study has highlighted the importance of IFNγ in the differentiation of CM into inflammatory CNS-resident MoMF [67], in line with a report on pathogenic *Cxcl10*$^+$ CM emerging during autoimmune neuroinflammation [68]. Finally, Goodridge and colleagues recently reported a DCMo accumulation in aged mice, as assessed by transcriptional profiling and MHC-II surface expression [69,70]. Collectively, these data and our findings suggest that DCMo might be the true ‘inflammatory’ monocytes emerging only upon specific inflammatory stimuli and with aging. Clearly, DCMo require further in-depth study with an unequivocal delineation from cDC and their precursors.

The main homeostatic function of monocytes is arguably the differentiation into monocyte-derived tissue resident macrophages. The competitive adoptive cell transfer

experiments performed in this study establish equal contributions of NeuMo and DCMo to NCM and gut macrophages, although it remains to be defined whether NeuMo and DCMo progeny are identical. In contrast, DCMo preferentially gave rise to lung IM. Moreover, DCMo-derived IM had higher surface expression of MHC-II, indicative of CM heterogeneity translating to tissue resident macrophage compartments. Intriguingly, we observed persistence of CD16.2^{+} precursors 12 days after transfer in the lung. These cells were previously hypothesized to be closely related to NCM [23]. However, graft-derived NCM were barely present in the blood on day 12 after transfer. Thus, at least with respect to their half-life, lung resident CD16.2^{+} precursors are distinct from NCM and warrant further study.

Deep sequencing revealed profound differences between DCMo- and NeuMo-derived IM, among which *H2-Aa* expression. Conversely, NeuMo-derived IM expressed gene modules involved in vasculature development and wound healing. The latter related to an earlier notion that linked Chil3^{+} monocytes to the resolution of inflammation [71]. Indeed, *Chil3* was higher expressed in NeuMo-IM compared to DCMo-IM. Importantly, stratification of DEG according to a proposed dichotomy of Lyve1^{high}MHC-II^{low} and Lyve1^{-}MHC-II^{high} macrophages across tissues [58] revealed NeuMo-IM and DCMo-IM to fall into the former and latter categories, respectively. This finding could add to the interpretation of heterogeneity of tissue resident macrophages.

Finally, NeuMo but not DCMo gave in the adoptive transfer experiment rise to dura mater macrophages. The exact mechanism for this selection remains to be defined. However, NeuMo differentially express CD62L and we show that administration of αCD62L antibody prior to transfer of NeuMo significantly prevented engraftment. While the nature of the CD62L ligand in the dura mater remains to be defined, differential adhesion molecule expression by NeuMo might also confer selective extravasation to other peripheral tissues.

A limitation of this study is the arguably artificial nature of the cell transfer model, involving the DTR-based macrophage ablation model. However, in steady state blood NeuMo are vastly abundant over DCMo, and the engraftment approach with equal numbers of NeuMo and DCMo, was hence needed to compare the potential fates of the cells.

What's in a name? Combined with the earlier seminal work [26,27] we establish here that the murine CM compartment comprises two subsets that are derived from GMP and MDP and display neutrophil- and DC-like transcriptomic signatures, respectively. Goodridge and Klein introduced the neutrophil- like and DC-like dichotomy and we decided to adopt it and not to suggest other names. We show in this study that NeuMo display activities associated with neutrophils, such as ET formation and recruitment by fMLP. However, the DCMo term implies a function that currently lacks support by experimental evidence.

In conclusion, we have identified surface markers that delineate murine CM subsets that share distinct neutrophil and DC features, in line with previous reports [26,27]. We

demonstrate that NeuMo and DCMo are *bona fide* monocytes that recirculate in the blood and have the capacity to give rise to tissue resident macrophages. Surprisingly though, NeuMo and DCMo show distinct homing and differentiation patterns to and in peripheral tissues, such as the lung and meninges. Our data point towards a model of specialized niches for ontogenically distinct monocytes and suggest that NeuMo and DCMo, whose abundance changes under challenge, give rise to transcriptionally and functionally distinct tissue resident macrophage subsets.

Data deposit

Gene expression data sets are deposited at GEO (Accession # xxxx)

Supplementary Data

Suppl Table 1. List of CITE-seq antibodies used in this study

Author contributions

S. T. and S. J. conceived the project and designed experiments. S.T., J-S. K., N. L., J. B., M. H., D. A., and M. G-V. performed experiments. S. T., J-S. K., and N. L. analyzed experiments. S. T. performed the bulk RNAseq and bioinformatic analysis. J. B. performed the single-cell experiment. D. K., J. B., and K. M. analyzed the single-cell experiment. J-S. K. and N. L. performed imaging experiments. S. T. performed adoptive cell transfers. S. T. and S. J. wrote the manuscript. S. J. supervised the project.

Acknowledgements

We would like to thank all members of the Jung laboratory, as well as the Jung lab alumni A. Mildner and S. Yona for advice and comments on the manuscript. We thank the staff of the Weizmann Animal and flow cytometry facilities. S.J is the incumbent of the Henry HG. Drake Professional Chair of Immunology. This research was generously supported by Morris Kahn Institute for Human Immunology. This project was funded by the Deutsche Forschungsgemeinschaft (DFG, German Research Foundation) – Project-ID 259373024 – TRR 167, and the Israeli Science Foundation (ISF) (grant # 696/21).

Figure legends

Figure 1: Identification and characterization of monocytes subsets by scRNAseq

(A) Experimental scheme for the CITE-seq experiment.

(B) Curated UMAP plot of the BM monocytes, DCs and their precursors identified by Cite-seq.

(C) UMAP plots showing the protein expression of Ly6C and CD115 as identified by CITE-seq antibodies, and Csf1r and *Fcgr3* gene expression in the dataset from B.

(D) UMAP plot, visualizing the mature monocyte and cDC subsets, and the gene or protein expression of selected markers.

(E) Differentially expressed genes between the CD177^{+} CM and CD319^{+} CM clusters identified by Cite-seq

(F) Dot plot showing specific upregulated genes (blue) and proteins (red) for the individual monocyte and cDC subsets as identified by Cite-seq. Dot size represents the percentage of cells expressing the gene and color represents its average expression.

(G) Gating on blood monocytes identifying CD177 and CD319 as markers for monocyte subsets. (n=12 from 8 independent experiments)

(H) Surface expression of canonical monocyte markers on CD177^{+} Ly6C^{high} CM (blue), CD319^{+} Ly6C^{high} CM (red), and CD177^{-}CD319^{-} Ly6C^{high} CM (black). (n=6 from 2-3 independent experiments)

Figure 2: Transcriptional characterization of blood CM subsets

(A) Volcano plot showing differentially expressed genes between CD177^{+} CM (blue dots) and CD319^{+} CM (red dots) from sorted blood cells subjected to bulk RNAseq. CM were defined as Lin^{-}CD11b^{+}CD115^{+}Cx3cr1^{GFP+}Ly6C^{high}CD11c^{-} cells. (n=4-5)

(B) Heatmap showing differentially expressed genes between DN (CD177^{-}CD319^{-} CM), CD177^{+} CM, and CD319^{+} CM from sorted blood cells. (n=4-5)

(C) Volcano plot of differentially expressed genes among CD177^{+}CD319^{-} CM and CD177^{-}CD319^{-} DN CM. (n=4-5)

(D) Scatter plots of selected genes among CD177^{+} CM, CD319^{+} CM, and DN CM. Selected ‘monocyte genes’ were not differentially expressed among subsets. (n=4-5)

(E) Metascape analysis of differentially expressed genes in CD177^{+} CM and CD319^{+} CM.

(F) Flow cytometry analysis of blood monocytes from *Ms4a3^{Cre}:R26-$^{LSL\text{-}TdTomato}$:Cx3cr1^{GFP}* mice. (n=6 from 2 independent experiments)

(G) Volcano plot of differentially expressed genes among *Ms3a4*^{Cre}*:R26*$^{LSL\text{-}TdTomato}$*-:Cx3cr1*^{GFP}+ (MDP-derived) monocytes and *Ms4a3*^{Cre}*:R26*$^{LSL\text{-}TdTomato}$*+:Cx3cr1*^{GFP}+ (GMP-derived) monocytes sorted from BM. CM were defined as CD11b^{+}CD115^{+}CD11c^{-}MHC-II^{-} Ly6C^{high} cells (n=5)

(H) Scatter plots of selected genes among BM GMP- and MDP-derived CM. Chil3, Frpr2, H2-Ab1, Cd209a, and Clec10a were differentially expressed. (n=5)

Figure 3: NeuMo and DCMo are preferentially represented upon distinct microbial stimuli

(A) Experimental scheme and blood analysis of LPS-treated mice one day after treatment. (n=9 from 3 independent experiments)

(B) Quantification of changes in the CM compartment after LPS treatment. (n=9 from 3 independent experiments)

(C) Histograms and quantification of changes in Cx$_3$cr1 and Sca1 surface expression among CM subsets following LPS treatment. (n=9 from 3 independent experiments)

(D) Experimental scheme and blood analysis of CpG-treated mice one day after treatment. (n=6 from 2 independent experiments)

(E) Quantification of changes in the CM compartment after CpG treatment. (n=6 from 2 independent experiments)

(F) Histograms and quantification of changes in Cx$_3$cr1 and Sca1 surface expression among CM subsets following CpG treatment. (n=6 from 2 independent experiments)

(G) Experimental scheme and blood analysis of IFNγ-treated mice one day after treatment. (n=6 from 2 independent experiments)

(H) Quantification of changes in the CM compartment after IFNγ treatment. (n=6 from 2 independent experiments)

(I) Histograms and quantification of changes in Cx$_3$cr1 and Sca1 surface expression among CM subsets following IFNγ treatment. (n=6 from 2 independent experiments)

Figure 4: NeuMo but not DCMo display distinct neutrophil-like functions *in vitro*

(A) Schematic of performed *in vitro* assays.

(B) Transcriptional expression of the formyl-methionine peptide receptor 2 (Fpr2) among CM subsets. (n=4-5)

(C) Quantification of migration of BM monocytes and neutrophils towards fMLP (100 nM) compared to control (DMSO), as assessed by flow cytometry. (n=6 from 2 independent experiments)

(D) Transcriptional expression of the protein amine deiminase 4 (Padi4) protein among CM subsets and intracellular staining for myeloperoxidase (MPO) among CM subsets by flow cytometry. (n=4-5 for transcriptomics, n=6 from 2 independent experiments for MPO staining)

(E) Quantification and microscopy images of the initiation of ETosis events as evidenced by co-staining for DNA, MPO, and citrullinated histone 3 (H3) as assessed by microscopy. (n=30-40 FOV of each cell type from 2 independent experiments)

(F) Quantification and representative flow cytometry plots of phagocytosis of GFP-expressing *Salmonella Typhimurium* by NeuMo and DCMo. (n=13 from 2 independent experiments)

Figure 5: NeuMo and DCMo give rise to NCM and intestinal macrophages

(A) Experimental scheme of adoptive transfer of $2x10^5$ NeuMo and DCMo, each. *Cx3cr1*^{DTR} chimeras were depleted of Cx_3cr1-expressing cells by repeated injection of 18 ng/g DTx / g bodyweight 8-10 weeks after chimerism. On day 0, CM subsets were adoptively co-transferred. Hereafter, mice were administered 12 ng/g DTx / g bodyweight every other day until sacrifice.

(B) Blood analysis of DTx- and PBS-treated *Cx3cr1*^{DTR} chimeras. (n=8)

(C) Blood analysis of circulating graft cells one day after adoptive transfer. (n=3)

(D) Blood analysis of circulating graft cells three days after adoptive transfer. (n=9)

(E) Quantification of surface marker expression on graft cells in the blood three days after transfer. (n=9)

(F) Microscopy images of graft-derived tissue resident macrophages in the colon and ileum of recipient animals. Scale bar = 80-100 um. (n=6 from 3 independent experiments)

(G) Flow cytometry analysis of graft-derived tissue resident macrophages in the colon and ileum of recipient animals. (n=4)

(H) Quantification of the distribution of graft-derived tissue resident macrophages in the colon and ileum of recipient animals. (n=7)

Figure 6: DCMo preferentially give rise to lung interstitial macrophages

(A) Representative microscopy image of CUBIC-cleared lungs showing graft-derived cells in the parenchyma.

(B) Flow cytometry plots of graft-derived cells in the lungs of recipient animals, and CD16.2 vs CD206 plots for each graft-derived population (n=6 from 2 independent experiments)

(C) Quantification of the contribution of DCMo- and NeuMo-derived populations to selected lung phagocyte populations, normalized to total number of graft-derived cells in the respective gates. (n=6 from 2 independent experiments)

(D) Foldchange in the ratio of mature IM to CD16.2^{+} precursors for DCMo- and NeuMo-derived graft cells. (n=6 from 2 independent experiments)

(E) Histogram plots and quantification of the surface expression of CD16.2 and MHC-II on CD206^{+} DCMo- and NeuMo-derived IM. (n=6 from 2 independent experiments)

(F) Volcano plot of differentially expressed genes among total DCMo- and NeuMo-derived phagocyte populations from the lung of recipient animals.

(G) Heatmap of selected differentially and non-differentially expressed genes attributed to Lyve1^{+}MHC-II^{low} and Lyve1^{-}MHC-II^{hi} IM as defined by Chakarov *et al.*

(H) Experimental scheme for adoptive transfer of GMP- and MDP-derived monocytes from *Ms4a3^{Cre}:R26$^{LSL\text{-}TdTomato}$:Cx3cr1^{GFP}* mice. *Cx3cr1^{DTR}* chimeras were depleted off Cx_3cr1-expressing cells by twice injection of 18 ng/g DTx / g bodyweight 8-10 weeks after chimerism. On day 0, CM subsets were adoptively co-transferred. Hereafter, mice were administered 12 ng/g DTx / g bodyweight every other day until sacrifice.

(I) Flow cytometry plots of graft-derived cells in the lungs of recipient animals, and CD16.2 vs CD206 plots for each graft-derived population. (n=6 from 2 independent experiments)

(J) Quantification of the contribution of MDP- and GMP-derived populations to selected lung phagocyte populations, normalized to total number of graft-derived cells in the respective gates. (n=6 from 2 independent experiments)

(K) Histogram plots and quantification of the surface expression of CD16.2, MHC-II, and Lyve1 on CD206^{+} MDP- and GMP-derived IM. (n=6 from 2 independent experiments)

Figure 7: NeuMo but not DCMo, give rise to meningeal dura mater macrophages

(A) Microscopy image of the dura mater of recipient mice 12 days after transfer. Both images depict the peripheral dura. Scale bars = 100 µm. (n=12 from 4 independent experiments)

(B) Microscopy image of the dura mater of recipient mice 21 days after transfer. Left: Sagittal sinus, right: periphery. Scale bars = 100 µm. (n=3)

(C) Microscopy image of the dura mater. NeuMo-derived BAM were stained for CD206 (green) and MHC-II (blue), 12 days after transfer. Scale bar = 100 µm. (n=3)

(D) Microscopy image of dura mater. NeuMo-derived BAM were stained for CD206 (green) and MHC-II (blue), 21 days after transfer. Scale bar = 80 µm. (n=2)

(E) Left: Schematic of the adoptive transfer experiment probing for the effect of CD62L on NeuMo recruitment to the dura mater. $2x10^5$ NeuMo were injected into each

mouse. Mice were administered aCD62L or isotype antibody (100 ug i.v., each) 1 hour before and 24 hours after cell transfer. Right: Normalized reads for *Sell*, encoding CD62L among blood CM subsets, as assessed by bulk RNAseq.

(F) Tile scans of the dura mater of aCD62L- and isotype-treated mice (left and middle) as well as quantification off total cell numbers detected in dura mater and colon in each treatment group (right). Scale bars = 1000 µm. (n=2-3)

Supplementary Figures

Supplemental Figure 1:

(A) UMAP plots of all identified BM cells. Monocytes, DCs and their precursors were selected and analyzed separately, as shown on the right.

(B) Marker genes of BM cell types.

(C) Expression of selected marker genes and proteins (the latter based on CITEseq antibodies) in tha dataset from A.

(D) Dot plot from the LEGENDscreen identifying CD319 as blood CM marker. Histograms for Cx_3cr1 and Ly6C shown as a validation for differences to CD177+ cells.

(E) Gating strategy for identification of blood immune subsets.

(F) Histograms showing the expression of CD177 and CD319 among blood immune subsets. (n=4)

(G) Distribution of selected markers for NeuMo and DCMo on CM subsets as predicted by Weinreb et al. (n=3-5)

(H) Table of NeuMo / DCMo markers showing log2 FC and adjusted p-value as adapted from Weinreb *et al*.

(I) Gating strategy for $CD177^+$ and $CD319^+$ from the VIB mouse facility in Brussels, Belgium. (n=3)

(J) Expression of CD88a and CD157 on NeuMo and DCMo in the blood. (n=3)

(K) Gating strategy for identification of a possible contamination of $Zbtb46^+Flt3^+$ cells in the blood CM gate used in this study. (n=3)

(L) Histograms showing the distribution of DC and monocyte markers on monocyte and DC subsets in the blood. (n=3)

Supplemental Figure 2

(A) Gating strategy for sorting CM subsets from the blood of $Cx3cr1^{GFP/+}$ mice for bulk RNAseq. (n=4-5)

(B) Venn diagram of DEG genes among CM subsets from this study and DEG from Weinreb et al.

(C) Histograms for differentially expressed surface markers in our bulk RNAseq dataset. (n=3)

(D) Reanalysis of a scRNAseq dataset on total blood monocytes.

(E) Gating strategy for sorting GMP- and MDP-derived CM from the BM of $Ms4a3^{Cre}:R26^{LSL\text{-}TdTomato}:Cx3cr1^{GFP}$ mice. (n=4)

(F) Heatmap of all DEG among GMP- and MDP-derived BM CM.

(G) Venn diagram of DEG among GMP- and MDP-derived BM CM and blood NeuMo and DCMo.

Supplementary Figure 3

(A) Gating strategy for BM monocyte precursors.
(B) Gating strategy for PBS-treated mice in the LPS experiment. (n=9 from 3 independent experiments)
(C) Histograms for various markers on CM subsets in LPS-treated mice. (n=9 from 3 independent experiments)
(D) Quantification of BM monocyte precursors in PBS- (ctrl) and LPS-treated mice. (n=3)
(E) Histogram and quantification of Sca1 surface expression on BM monocyte precursors in ctrl and LPS-treated mice. (n=3)
(F) Histogram and quantification of Cx_3cr1 surface expression on BM monocyte precursors in ctrl and LPS-treated mice. (N=3)
(G) Gating strategy for PBS-treated mice in the CpG experiment. (n=6 from 2 independent experiments)
(H) Histograms for various markers on CM subsets in CpG-treated mice. (n=6 from 2 independent experiments)
(I) Quantification of BM monocyte precursors in PBS- (ctrl) and CpG-treated mice. (n=3)
(J) Histogram and quantification of Sca1 surface expression on monocyte precursors in ctrl and CpG-treated mice. (n=3)
(K) Histogram and quantification of Cx_3cr1 surface expression on monocyte precursors in ctrl and CpG-treated mice. (N=3)
(L) Gating strategy for PBS-treated mice in the IFNγ experiment. (n=6 from 2 independent experiments)
(M) Histograms for various markers on CM subsets in IFNγ-treated mice. (n=6 from 2 independent experiments)
(N) Experimental scheme for the sorting of $Sca1^+$ and $Sca1^-$ CM after IFNγ treatment on 3 consecutive days.
(O) Volcano plot of DEG genes among $Sca1^+$ and $Sca1^-$ CM from IFNγ-treated mice.
(P) Gene expression plots of selected genes from $Sca1^+$ and $Sca1^-$ CM from IFNγ-treated mice.
(Q) Heat map of DEG among CM from control and IFNg-treated mice.

Supplementary Figure 4

(A) Gating strategy for sorting NeuMo and DCMo from the BM for functional assays.

(B) Density plots of migrated cells from DMSO (ctrl) and fMLP wells. (n=6 from 2 independent experiments)

(C) Gating strategy for measuring engulfment of *S. Tm* in sorted NeuMo and DCMo. (n=13 from 2 independent experiments)

Supplementary Figure 5

(A) Gating strategy for lung IM.

(B) Blood of recipient mice on day 12 after transfer. Each plot represent a biological replicate.

(C) Expression of MHC-II on the surface of CD16.2^{+} precursors and CD206^{-} IM, including MFI quantification. (n=6 from 2 independent experiments)

(D) Gating strategy for sorting NeuMo- and DCMo-derived IM for bulk RNAseq analysis.

(E) Heatmap of the 30 top DEG from NeuMo- and DCMo-derived IM.

(F) Metascape analysis of DEG in NeuMo- and DCMo-derived IM.

(G) Gene plots for gene signatures of lung IM and precursors from Schyns *et al.*

(H) Gene plots for selected genes of interest among NeuMo- and DCMo-derived IM. Among 'NeuMo / DCMo markers', *Mmp8* and *H2-Aa* were differentially expressed.

Supplementary Figure 6

(A) Microscopy picture of the brain parenchyma of DTx-treated recipient mice. Scale bar = 100 µm. (n=3)

(B) Microscopy picture of the leptomeninges of DTx-treated recipient mice. Scale bar = 300 µm. (n=3)

(C) Tile scan of the dura mater of DTx-treated recipient mice. Scale bar = 500 µm. (n=1)

(D) Microscopy pictures of the dura mater of DTx-treated mice transferred with *Cx3cr1*^{GFP} NeuMo and *Cx3cr1*^{Cre}*:R26*$^{LSL\text{-}TdTomato}$ DCMo (2x10^{5} each). Scale bars = 80-100 µm. (n=3)

(E) Tile scans of the colons of isotype- and aCD62L-treated mice. Scale bars = 500-700 µm. (n=2-3)

Methods

Mice

This study involved the following animals, all on C57BL/6 background: wild type C57BL/6 mice (Harlan); *Cx3cr1*^{GFP} mice (B6.129P2(Cg)-*Cx3cr1*^{tm1Litt}/J) Jax stock #005582 [33]; *Cx3cr1*^{Cre} mice (B6J.B6N(Cg)-*Cx3cr1*$^{tm1.1(cre)/Jung}$/J) Jax stock #025524 [11]; *Cx3cr1*^{DTR} mice (B6N.129P2-*Cx3cr1*$^{tm3(DTR)Litt}$/J) Jax stock #025629 [52]; *Ms4a3*^{Cre} mice (C57BL/6J-*Ms4a3*$^{em2(cre)Fgnx}$/J) Jax stock #036382 [13]; *Rosa26*$^{LSL\text{-}TdTomato}$ (B6.Cg-*Gt(ROSA)26Sor*$^{tm9(CAG\text{-}tdTomato)Hze}$/J) Jax stock #007909 [72]. All transgenic mice were heterozygotes for the modified alleles. Male and female mice of 7-10 weeks were used in most experiments. For generation of BM chimeras, wild type C57BL/6 mice were used as recipients. Recipient mice were lethally irradiated with a single dose of 950 cGy using an XRAD 320 machine (Precision X-Ray) and reconstituted the next day by i.v. injection of 5 x 10^6 donor BM cells per mouse. Recipients were allowed to recover vor 8-10 weeks before performing experiments. All animals were maintained in a specific-pathogen-free facility with chow and water provided *ad libitum* and handled according to protocols approved by the Weizmann Institute Animal Care Committee as per international guidelines.

LPS, CpG, IFN, Antibody, and DTx Treatments

For the LPS challenge, mice were injected intraperitoneally (i.p.) or intravenously (i.v.) with a single dose of LPS (*E. coli* O111:B4; Sigma Cat#L2630) 2.5 mg/kg. For the CpG challenge, mice were injected i.v. with a single dose of CpG (ODN 1826, Class B CpG oligonucleotide, InvivoGen Cat#tlr-1826) 5 ug/mouse and DOTAP (DOTAP liposomal transfection reagent, Sigma-Aldrich Cat#890895P-25MG) 25 ug/mouse. For the IFNg challenge, mice were injected i.v. with a single dose or i.p. for 3 consecutive days with recombinant murine IFNg (Peprotech Cat#315-05) 5 ug/mouse. To assess the CD62L involvement in NeuMo trafficking to the dura mater, recipient mice were injected 1h prior to adoptive cell transfer i.v. with purified anti-mouse CD62L antibody (clone MEL-14, BioLegend Cat#104402) 100 ug/mouse or purified rat IgG2a,k isotype ctrl antibody (clone RTK2758, BioLegend Cat#400502) 100 ug/mouse. Injection was repeated once more 24h after the initial injection. For depletion of Cx3cr1-expressing cells in *Cx3cr1*^{DTR} chimeras, two initial doses of diphtheria toxin (*C. diphtheria*, Sigma Cat#D0564-1MG) 18 ng/g bodyweight per day were given before adoptive cell transfer. After cell transfer, 12 ng/g bodyweight DTx was administered every other day.

Cell Isolation from Tissue for Flow Cytometry

Peripheral blood was collected through cardiac puncture or cheek punch. RBC were lyzed by home-made ACK buffer. Cell suspensions were then resuspended in home-made FACS buffer (2% FCS, 1 mM EDTA). Cells were stained with biotinylated lineage markers TCRb (clone H57-597), CD19 (clone 6D5), NK1.1 (clone PK136). The backbone surface panel consisted of CD11b (clone M1/70), CD115 (clone AFS98), Ly6C (clone HK1.4), CD11c (clone N418), CD319 (clone 4G2), CD177 (clone Y127), I-A/I-E (clone M5/114.15.2), CX3CR1 (clone SA011F11). Additional markers were integrated into this panel as necessary. Single cells suspensions were filtered and acquired on a Cytek Aurora 4L spectral cytometer (16V-14B-10YG-8R, Cytek Biosciences).

Lungs were perfused, tissue was collected and weighed. Tissue was transferred to digestion solution (RPMI + 1 mg/ml Col IV + 0.02 mg/ml DNase I) and minced into fine pieces. This was incubated on a shaker for 30 min at 37°C at 200 rpm. The pellet was disrupted after 15 min of incubation. After 30 min, the suspension was pipetted until homogenized and filtered through a 40 um cell strainer. The cell suspension was washed with PBS + 1mM EDTA before spinning down. The resulting pellet was then stained. Surface markers used for lung experiments included: CD45 (clone 30-F11), CD11b (clone M1/70), CD64 (clone X54-5/7.1), I-A/I-E (clone M5/114.15.2), SiglecF (clone S17007L), CD11c (clone N418), CX3CR1 (clone SA011F11), Lyve1 (clone ALY7), CD16.2 (clone 9E9), CD206 (clone C068C2).

For analysis of colon and ileum, cells were isolated as previously described [55].

Adoptive Cell Transfers

Femurs, tibias, and spine of donor mice were removed. BM was extracted by crushing the bones. All subsequent steps were carried out on ice. Cells were centrifuged and incubated with biotin-labeled anti-CD115 (clone AFS98, 1:200) for 20 minutes. After a washing step, cells were incubated with Streptavidin Microbeads (30-50 ul per mouse, Miltenyi Biotec). After another wash, magnetic separation was performed according to the manufacturer's instructions. Positively selected cells (CD115+) were stained with Ly6C, CD11b, CD115, and CD177 and CD319 depending on th experiment. Cells were sorted on FACS Aria III (BD Biosciences) into cold RPMI + 10% FCS. Cells were spun down and counted. $2x10^5$ cells of each cell type were injected i.v. into DTx-depleted recipients.

ETosis Assay

To induce ET formation, cells were isolated as previously described in 'Adoptive Cell Transfers'. Freshly sorted 1 x 10^5 cells were resuspended in RPMI medium 1640 containing 100 nM PMA, and plated on Cell-tak coated coverslips for 6 hours at 37°C. Then, medium was aspirated and cells were fixed at RT with 4% PFA for 10 min, blocked and

permeabilized using PBS with 0.1% Triton X-100, 1% fetal calf serum, and 5% BSA for 30 min. Cells were then stained for citrullinated H3, MPO, and DNA (DAPI). Cover slips were imaged using an Olympus BX51 confocal laser scanning microscope, and analyzed using Fiji. 15-20 FOV for each cell subset were selected and triple-positive events were counted and normalized to all DAPI$^+$ events.

Transwell Migration Assay

Cells were isolated as detailed in 'Adoptive Cell Transfers' without staining and sorting steps. Importantly, for this experiment, all steps were carried out at room temperature. Transwells (24-well plate, 6.5mm diameter transwell, 5 um pore size, Costar) were pre-coated with 1% BSA at 37°C for 1 hour and then washed twice with PBS. Cells were washed twice in PBS and resuspended in binding medium (HBSS, 1% PSA, 1% HEPES, 1mM CaCl2, 2 mg/ml BSA). 100 nM of fMLP or equivalent volume of DMSO were gently resuspended in pre-warmed binding medium and 600 ul were put in the bottom well. 100 ul of cell suspension (5e6 cells/ml) were seeded in the transwell filter. Cells were let migrate for one hour at 37°C. Then, transwells were removed, medium was collected from the lower well. Cells were spun down and stained with CD11b, CD115, Ly6C, CD177, and CD319. Finally, cell suspensions were acquired on a Cytek Aurora 4L spectral cytometer.

Phagocytosis Assay

Cells were isolated as detailed in 'Adoptive Cell Transfers' and incubated with GFP-expressing *Salmonella Typhimurium* in a 10:1 ratio for 2 hours at 37°C. Then, gentamycin was added for 5 minutes before spinning down. Finally, cells were acquired on a Cytek Aurora 4L spectral cytometer.

Histology

Recipient mice were anesthetized with Pental and perfused with cold PBS. The dura mater was detached from the skull. Brain tissues were excised and fixed for 2 hours in 4% PFA at RT. Whole-mount pre-fixed tissues were blocked in 2% horse serum for 2h at RT and incubated with primary antibody overnight at 4°C. After incubation, tissues were washed thrice in PBS and incubated with secondary antibody for 2h at RT. Subsequently, tissues were incubated for 5 min with DAPI (1:10k) (Sigma), and washed thrice with PBS. Tissues were recorded with a Zeiss LSM 880 confocal laser scanning microscope with ZEN microscopy software. Image analysis was processed by Imaris software (Oxford Instruments). The following primary antibodies were used: rat monoclonal anti-CD31 (1:250, MEC13.3, Biolegend, #102502), goat polyclonal anti-CD206 (1:250, R&D Systems, #AF2535), rat monoclonal anti-MHC class II (I-A/I-E) (1:250, M5.114.15.2, Invitrogen #14-

5321-82), and following secondary antibodies were used: donkey anti-rat IgG (H+L) cy3 (cat. no. 712-165- 154), and donkey anti-goat IgG (H+L) Alexa Fluor 647 (cat. no. 705-605-147), which are all from Jackson Immuno Research Laboratory (JIR).

Cubic Clearing

For cubic clearing, lungs were perfused with cold PBS. A slightly modified protocol of Matsumoto *et al* [73] was followed. Briefly, samples were incubated in CUBIC 1 solution : PBS (50:50) overnight at RT on a shaker. Then, samples were incubated in 100% CUBIC 1 solution for at least 3 days. Samples were then moved to CUBIC 2 solution: PBS (50:50) for overnight incubation at RT on a shaker. Following, samples were incubated in 100% CUBIC 2 solution for 2 days at 37°C on a shaker (100 rpm). After 2 days, samples were stored in mineral oil (Sigma M8410) and imaged the next day.

CITE-seq Library Generation and Analysis

The femur was harvested from a 10 week-old C57BL6 female mouse. The BM was placed directly into ice-cold Roswell park Memorial Institute (RPMI) 1640 medium (Thermofisher). No actinomycin D was used as there were no tissue digestion steps present and all steps were performed with ice-cold buffers to maintain the cells at a low temperature. The BM was flushed by cutting the femur in two and flushing the bone cavity with a syringe with a 26g needle filled with 5% magnetic-activated cell sorting (MACS) buffer (5% inactivated fetal calf serum, 2mM EDTA (Duchefa), 1X Hanks' buffered salt solution (HBSS) (Gibco)). This BM was flushed through a 40µm cell strainer (Corning) and the filter was washed with 5% MACS buffer. The BM was centrifuged at 450g for 6 minutes at 4°C. The supernatant was discarded, and the pellet was resuspended in home-made RBC lysis buffer. The lysis buffer was neutralized with 5% MACS buffer and the cell suspension was centrifuged. The pellet was resuspended, counted with trypan blue, and 925,000 cells were aliquoted and centrifuged. The supernatant was discarded and the cell pellet was resuspended in 25µl 1X PBS with 0.04% bovine serum albumin (BSA) buffer, containing mouse TruStain FcX (BioLegend) and the mouse cell surface protein antibody panel containing 174 oligo-conjugated antibodies (**Supplementary Table 1**). The cells were stained for 30 minutes on ice, followed by a washing step before loading. Single-cell suspensions were loaded on a GemCode Single Cell Instrument (10× Genomics) to generate single-cell gel beads in emulsion (GEM) using a GemCode Single Cell 3′ Gel Bead and Library kit v.3.1 (10x Genomics, 1000121) and a Chromium i7 Multiplex Kit (10× Genomics, 120262) as previously described [74]. Briefly, GEM reverse-transcription incubation was performed in a 96-deep-well reaction module at 53°C for 45 min, 85°C for 5 min and ending at 4°C. Next, GEMs were broken and complementary DNA (cDNA) was cleaned up with DynaBeads

MyOne Silane Beads (10x Genomics, No. 2000048) and SPRIselect Reagent Kit (Beckman Coulter, No. B23318). Full-length, barcoded cDNA was PCR amplified with a 96-deep-well reaction module at 98°C for 3 min, 11 cycles at 98°C for 15 s, 63°C for 20 s and 72°C for 1 min, followed by one cycle at 72°C for 1 min and ending at 4°C. Following cleaning up with the SPRIselect Reagent Kit and enzymatic fragmentation, library construction to generate Illumina-ready sequencing libraries was performed by the addition of R1 (read 1 primer), P5, P7, i7 sample index and R2 (read 2 primer sequence) via end-repair, A-tailing, adapter ligation, post-ligation SPRIselect cleanup/size selection and sample index PCR. The cDNA content of pre-fragmentation and post-sample index PCR samples was analyzed using the 2100 BioAnalyzer (Agilent). Sequencing libraries were loaded on an Illumina Illumina NovaSeq 6000 flow cell, with sequencing settings according to the recommendations of 10× Genomics (read 1: 26 cycles; read 2: 98 cycles; index i7: eight cycles; index i5: no cycles, pooled in a 80:20 ratio for the combined 3′ gene expression and cell surface protein samples, respectively). The Cell Ranger software (10x Genomics) was used to perform sample demultiplexing, RNA read mapping to the reference genome (mouse mm10) and RNA and ADT barcode processing, unique molecular identifiers filtering and single-cell UMI counting. The mean of the mapped RNA reads per cell was 18 864, with a sequencing saturation of 41.3%, as calculated by Cell Ranger. The ADT libraries yielded 1186 mean reads per cell, and 52.1% ADT sequencing saturation. The RNA expression matrix was further filtered and preprocessed using the Seurat (v.4.0.5) and Scater (v.1.22.0) R packages. For filtering the low-quality cell barcodes, associated with droplets that do not contain intact cells, the “emptyDrops” function of the DropletUtils package (v.1.14.2) has been applied on the RNA expression data, using an FDR cutoff of 0.01. Outlier cells were additionally identified based on three metrics (library size, number of expressed genes and mitochondrial proportion per cell); cells were tagged as outliers, when they were more than three median absolute deviations distant from the median value of each metric across all cells. Doublet score was assigned to each cell barcode based on generation of cluster-based artificial doublets with the scDblFinder function of the scDblFinder package (1.8.0). Low-abundance genes were removed using the Scater ‘calcAverage’ function and a cutoff of 0.003 mean reads per gene. The resulting RNA matrix was normalized using the global-scaling normalization and log-transformation ‘LogNormalize’ Seurat function. To mitigate the effects of cell cycle heterogeneity on the dataset, we calculating cell cycle phase scores based on canonical S and G2/M markers using the CellCycleScoring function of Seurat. Next, the cell cycle scores were regressed out from the data. Highly variable genes were detected in Seurat and the gene expression was scaled by linear transformation. Subsequently, the identified highly variable genes were used for performing principal component analysis (PCA). The PCA embeddings were used downstream for unsupervised

Leiden clustering of the cells and Uniform Manifold Approximation and Projection (UMAP) dimensionality reduction as implemented in Seurat. Differential gene expression analysis was done using Wilcoxon Rank Sum test and Bonferroni correction has been applied for adjustment of the P values. Several of the identified clusters were further individually subsetted and re-clustered in order to obtain a more refined mapping of the murine BM subpopulations. During this process, we iteratively excluded cell subclusters that showed both high doublet score and expression of markers, specific for two different cell populations, e.g., of the neutrophil markers Ly6g/S100a8 and the B cell markers Cd19/Cd79a. The total number of identified cells after removing artefacts and cell doublets was 16066.The processing of the ADT expression matrix was done as described previously [74]. In brief, the ADT cell barcodes, associated with artefact cells based on the RNA expression analysis were discarded, and the remaining data was normalized using the ASINH_GEOM transformation (inverse hyperbolic sine transformation with a cofactor).

RNAseq Library Preparation

Peripheral blood or lung cells were isolated as previously described and sorted into 30 ul of lysis/binding buffer (home-made or Life Technologies) and stored at -80°C. mRNA was then captured with Dynabeads oligo(dT) (Life Technologies) according to the manufacturer's guidelines. A bulk variation of MARSseq [75] was used for preparation of RNAseq libraries. Briefly, RNA was first reverse-transcribed with MARSseq barcoded RT primers with the Affinity Script kit (Agilent). Reverse transcription was analyzed by qRT-PCR and samples with a similar CT were pooled. Each pool was treated with Exonuclease I (NEB) for 30' at 37°C. Double-stranded DNA was generated with the NEB second strand synthesis kit at 16°C for 2h.), Subsequently, *in vitro* transcription was performed over-night with the T7 High Yield RNA polymerase IVT kit (NEB) for 37°C overnight. Following IVT, the DNA template was removed with Turbo DNase I (Ambion) at 37°C for 15'. Amplified RNA was fragmented by incubation at 70°C for 3' in Zn2+ RNA fragmentation reagent (Ambion). RNA was then ligated to the MARSseq ligation adaptor with T4 RNA Ligase I (NEB) at 22°C for 2h. Ligated product was reverse-transcribed using the Affinity Script RT enzyme (Agilent) and a primer complementary to the ligated product. The library was completed and amplified through a nested PCR reaction with P5_Rd1 and P7_Rd2 primers and PCR ready mix (Kappa Biosystems). Library concentrations was measured with a Qubit fluorometer (Life Technologies) and mean molecule size was determined with a 2200 TapeStation instrument. RNAseq libraries were sequenced using the Illumina NextSeq 500.

RNAseq analysis

Data analysis was performed using the UTAP transcriptome analysis pipeline [76].Raw reads were trimmed using cutadapt with the parameters: -a AGATCGGAAGAGCACACGTCTGAACTCCAGTCAC -a ‘‘A–times 2 -u 3 -u 3 -q 20 -m 25). Reads were mapped to the genome (mm10, Gencode annotation version 10.0) using STAR (v2.4.2a) with the parameters –alignEndsType EndToEnd, –outFilterMismatchNoverLmax 0.05, –twopassMode Basic, –alignSoftClipAtReferenceEnds No. The pipeline quantifies the 30 of Gencode annotated genes (The 30 region contains 1,000 bases upstream of the 30 end and 100 bases downstream). UMI counting was done after marking duplicates (in-house script) using HTSeq-count in union mode. Only reads with unique mapping were considered for further analysis, and genes having minimum 5 reads in at least one sample were considered. Gene expression levels were calculated and normalized using DESeq2 with the parameters: betaPrior=True, cooksCutoff=FALSE, independentFilter- ing=FALSE. Batch correction was done using the *sva* (3.26.0) R when batch adjustments were required. Raw p-values were adjusted for multiple testing, using the procedure of Benjamini and Hochberg. Differentially expressed genes were selected with absolute fold change (log2)>1, and adjusted p-value <0.05. Visualization of gene expression heatmaps was done using Gene-e, using log normal- ized values. Clustering was applied on log2 transformed and standardized expression values, using the k-means algorithm (Euclidian method). For Gene Ontology (GO) term analysis, Metascape was used [37], and all heatmaps were made by Morpheus, https://software.broadinstitute.org/morpheus.

Statistical Analysis

In all experiment, data are presented as mean +- standard deviation (SD). Statistical tests were selected based on appropriate assumptions with respect to data distribution and variance characteristics. Student’s t test (two-tailed) was applied to demonstrate statistical differences between two groups, and Two-way ANOVA was used when appropriate. Sample sizes were chosen according to standard guidelines. Number of animals is indicated as ‘‘n’’ and presented with the number of dots on the graphs.

References

1. Guilliams, M., Mildner, A., and Yona, S. (2018). Developmental and Functional Heterogeneity of Monocytes. Immunity *49*, 595–613. 10.1016/j.immuni.2018.10.005.

2. Hettinger, J., Richards, D.M., Hansson, J., Barra, M.M., Joschko, A.-C., Krijgsveld, J., and Feuerer, M. (2013). Origin of monocytes and macrophages in a committed progenitor. Nat Immunol *14*, ni.2638. 10.1038/ni.2638.

3. Yáñez, A., Ng, M.Y., Hassanzadeh-Kiabi, N., and Goodridge, H.S. (2015). IRF8 acts in lineage-committed rather than oligopotent progenitors to control neutrophil vs monocyte production. Blood *125*, 1452–1459. 10.1182/blood-2014-09-600833.

4. Ginhoux, F., and Jung, S. (2014). Monocytes and macrophages: developmental pathways and tissue homeostasis. Nat Rev Immunol *14*, 392–404. 10.1038/nri3671.

5. Passlick, B., Flieger, D., and Ziegler-Heitbrock, H. (1989). Identification and characterization of a novel monocyte subpopulation in human peripheral blood. Blood *74*, 2527–2534. 10.1182/blood.v74.7.2527.bloodjournal7472527.

6. Palframan, R.T., Jung, S., Cheng, G., Weninger, W., Luo, Y., Dorf, M., Littman, D.R., Rollins, B.J., Zweerink, H., Rot, A., et al. (2001). Inflammatory chemokine transport and presentation in HEV: a remote control mechanism for monocyte recruitment to lymph nodes in inflamed tissues. The Journal of experimental medicine *194*, 1361–1373.

7. Geissmann, F., Jung, S., and Littman, D.R. (2003). Blood monocytes consist of two principal subsets with distinct migratory properties. Immunity *19*, 71–82. 10.1016/s1074-7613(03)00174-2.

8. Trzebanski, S., and Jung, S. (2020). Plasticity of Monocyte Development and Monocyte Fates. Immunol Lett *227*, 66–78. 10.1016/j.imlet.2020.07.007.

9. Auffray, C., Fogg, D., Garfa, M., Elain, G., Join-Lambert, O., Kayal, S., Sarnacki, S., Cumano, A., Lauvau, G., and Geissmann, F. (2007). Monitoring of Blood Vessels and Tissues by a Population of Monocytes with Patrolling Behavior. Science *317*, 666–670. 10.1126/science.1142883.

10. Mildner, A., Schönheit, J., Giladi, A., David, E., Lara-Astiaso, D., Lorenzo-Vivas, E., Paul, F., Chappell-Maor, L., Priller, J., Leutz, A., et al. (2017). Genomic Characterization of Murine Monocytes Reveals C/EBPβ Transcription Factor Dependence of Ly6C− Cells. Immunity *46*, 849-862.e7. 10.1016/j.immuni.2017.04.018.

11. Yona, S., Kim, K.-W., Wolf, Y., Mildner, A., Varol, D., Breker, M., Strauss-Ayali, D., Viukov, S., Guilliams, M., Misharin, A., et al. (2013). Fate Mapping Reveals Origins and Dynamics of Monocytes and Tissue Macrophages under Homeostasis. Immunity *38*, 79–91. 10.1016/j.immuni.2012.12.001.

12. Patel, A.A., Zhang, Y., Fullerton, J.N., Boelen, L., Rongvaux, A., Maini, A.A., Bigley, V., Flavell, R.A., Gilroy, D.W., Asquith, B., et al. (2017). The fate and lifespan of human monocyte subsets in steady state and systemic inflammation. The Journal of experimental medicine *74*, jem.20170355-11. 10.1084/jem.20170355.

13. Liu, Z., Gu, Y., Chakarov, S., Bleriot, C., Kwok, I., Chen, X., Shin, A., Huang, W., Dress, R.J., Dutertre, C.-A., et al. (2019). Fate Mapping via Ms4a3-Expression History Traces Monocyte-Derived Cells. Cell *178*, 1509-1525.e19. 10.1016/j.cell.2019.08.009.

14. Menezes, S., Melandri, D., Anselmi, G., Perchet, T., Loschko, J., Dubrot, J., Patel, R., Gautier, E.L., Hugues, S., Longhi, M.P., et al. (2016). The Heterogeneity of Ly6Chi Monocytes Controls Their Differentiation into iNOS+ Macrophages or Monocyte-Derived Dendritic Cells. Immunity *45*, 1205–1218. 10.1016/j.immuni.2016.12.001.

15. Briseño, C.G., Haldar, M., Kretzer, N.M., Wu, X., Theisen, D.J., KC, W., Durai, V., Grajales-Reyes, G.E., Iwata, A., Bagadia, P., et al. (2016). Distinct Transcriptional Programs Control Cross-Priming in Classical and Monocyte-Derived Dendritic Cells. Cell Rep. *15*, 2462–2474. 10.1016/j.celrep.2016.05.025.

16. Cheong, C., Matos, I., Choi, J.-H., Dandamudi, D.B., Shrestha, E., Longhi, M.P., Jeffrey, K.L., Anthony, R.M., Kluger, C., Nchinda, G., et al. (2010). Microbial Stimulation Fully Differentiates Monocytes to DC-SIGN/CD209+ Dendritic Cells for Immune T Cell Areas. Cell *143*, 416–429. 10.1016/j.cell.2010.09.039.

17. Auffray, C., Fogg, D.K., Narni-Mancinelli, E., Senechal, B., Trouillet, C., Saederup, N., Leemput, J., Bigot, K., Campisi, L., Abitbol, M., et al. (2009). CX3CR1+ CD115+ CD135+ common macrophage/DC precursors and the role of CX3CR1 in their response to inflammation. J. Exp. Med. *206*, 595–606. 10.1084/jem.20081385.

18. Varol, C., Landsman, L., Fogg, D.K., Greenshtein, L., Gildor, B., Margalit, R., Kalchenko, V., Geissmann, F., and Jung, S. (2007). Monocytes give rise to mucosal, but not splenic, conventional dendritic cells. J Exp Medicine *204*, 171–180. 10.1084/jem.20061011.

19. Gamrekelashvili, J., Giagnorio, R., Jussofie, J., Soehnlein, O., Duchene, J., Briseño, C.G., Ramasamy, S.K., Krishnasamy, K., Limbourg, A., Häger, C., et al. (2016). Regulation of monocyte cell fate by blood vessels mediated by Notch signalling. Nat. Commun. *7*, 12597. 10.1038/ncomms12597.

20. Gamrekelashvili, J., Kapanadze, T., Sablotny, S., Ratiu, C., Dastagir, K., Lochner, M., Karbach, S., Wenzel, P., Sitnow, A., Fleig, S., et al. (2020). Notch and TLR signaling coordinate monocyte cell fate and inflammation. eLife *9*, e57007. 10.7554/elife.57007.

21. Carlin, L.M., Stamatiades, E.G., Auffray, C., Hanna, R.N., Glover, L., Vizcay-Barrena, G., Hedrick, C.C., Cook, H.T., Diebold, S., and Geissmann, F. (2013). Nr4a1-Dependent Ly6Clow Monocytes Monitor Endothelial Cells and Orchestrate Their Disposal. Cell *153*, 362–375. 10.1016/j.cell.2013.03.010.

22. Landsman, L., Bar-On, L., Zernecke, A., Kim, K.-W., Krauthgamer, R., Shagdarsuren, E., Lira, S.A., Weissman, I.L., Weber, C., and Jung, S. (2009). CX3CR1 is required for monocyte homeostasis and atherogenesis by promoting cell survival. Blood *113*, 963–972. 10.1182/blood-2008-07-170787.

23. Schyns, J., Bai, Q., Ruscitti, C., Radermecker, C., Schepper, S.D., Chakarov, S., Farnir, F., Pirottin, D., Ginhoux, F., Boeckxstaens, G., et al. (2019). Non-classical tissue monocytes and two functionally distinct populations of interstitial macrophages populate the mouse lung. Nat Commun *10*, 3964. 10.1038/s41467-019-11843-0.

24. Evren, E., Ringqvist, E., Tripathi, K.P., Sleiers, N., Rives, I.C., Alisjahbana, A., Gao, Y., Sarhan, D., Halle, T., Sorini, C., et al. (2020). Distinct developmental pathways from blood

monocytes generate human lung macrophage diversity. Immunity. 10.1016/j.immuni.2020.12.003.

25. Hoffman, D., Tevet, Y., Trzebanski, S., Rosenberg, G., Vainman, L., Solomon, A., Hen-Avivi, S., Ben-Moshe, N.B., and Avraham, R. (2021). A non-classical monocyte-derived macrophage subset provides a splenic replication niche for intracellular Salmonella. Immunity *54*, 2712-2723.e6. 10.1016/j.immuni.2021.10.015.

26. Yáñez, A., Coetzee, S.G., Olsson, A., Muench, D.E., Berman, B.P., Hazelett, D.J., Salomonis, N., Grimes, H.L., and Goodridge, H.S. (2017). Granulocyte-Monocyte Progenitors and Monocyte-Dendritic Cell Progenitors Independently Produce Functionally Distinct Monocytes. Immunity *47*, 890-902.e4. 10.1016/j.immuni.2017.10.021.

27. Weinreb, C., Rodriguez-Fraticelli, A., Camargo, F.D., and Klein, A.M. (2020). Lineage tracing on transcriptional landscapes links state to fate during differentiation. Science, eaaw3381. 10.1126/science.aaw3381.

28. Ikeda, N., Kubota, H., Suzuki, R., Morita, M., Yoshimura, A., Osada, Y., Kishida, K., Kitamura, D., Iwata, A., Yotsumoto, S., et al. (2023). The early neutrophil-committed progenitors aberrantly differentiate into immunoregulatory monocytes during emergency myelopoiesis. Cell Reports *42*, 112165. 10.1016/j.celrep.2023.112165.

29. Wolf, A.A., Yáñez, A., Barman, P.K., and Goodridge, H.S. (2019). The Ontogeny of Monocyte Subsets. Front Immunol *10*, 1642. 10.3389/fimmu.2019.01642.

30. Anderson, D.A., Dutertre, C.-A., Ginhoux, F., and Murphy, K.M. (2020). Genetic models of human and mouse dendritic cell development and function. Nat Rev Immunol, 1–15. 10.1038/s41577-020-00413-x.

31. Meredith, M.M., Liu, K., Kamphorst, A.O., Idoyaga, J., Yamane, A., Guermonprez, P., Rihn, S., Yao, K.-H., Silva, I.T., Oliveira, T.Y., et al. (2012). Zinc finger transcription factor zDC is a negative regulator required to prevent activation of classical dendritic cells in the steady state. J Exp Med *209*, 1583–1593. 10.1084/jem.20121003.

32. Satpathy, A.T., KC, W., Albring, J.C., Edelson, B.T., Kretzer, N.M., Bhattacharya, D., Murphy, T.L., and Murphy, K.M. (2012). Zbtb46 expression distinguishes classical dendritic cells and their committed progenitors from other immune lineages. J Exp Med *209*, 1135–1152. 10.1084/jem.20120030.

33. Jung, S., Aliberti, J., Graemmel, P., Sunshine, M.J., Kreutzberg, G.W., Sher, A., and Littman, D.R. (2000). Analysis of Fractalkine Receptor CX3CR1 Function by Targeted Deletion and Green Fluorescent Protein Reporter Gene Insertion. Mol. Cell. Biol. *20*, 4106–4114. 10.1128/mcb.20.11.4106-4114.2000.

34. Cassatella, M.A., Östberg, N.K., Tamassia, N., and Soehnlein, O. (2019). Biological Roles of Neutrophil-Derived Granule Proteins and Cytokines. Trends Immunol *40*, 648–664. 10.1016/j.it.2019.05.003.

35. Othman, A., Sekheri, M., and Filep, J.G. (2022). Roles of neutrophil granule proteins in orchestrating inflammation and immunity. Febs J *289*, 3932–3953. 10.1111/febs.15803.

36. Tamura, A., Hirai, H., Yokota, A., Kamio, N., Sato, A., Shoji, T., Kashiwagi, T., Torikoshi, Y., Miura, Y., Tenen, D.G., et al. (2017). C/EBPβ is required for survival of Ly6C− monocytes. Blood *130*, 1809–1818. 10.1182/blood-2017-03-772962.

37. Zhou, Y., Zhou, B., Pache, L., Chang, M., Khodabakhshi, A.H., Tanaseichuk, O., Benner, C., and Chanda, S.K. (2019). Metascape provides a biologist-oriented resource for the analysis of systems-level datasets. Nat Commun *10*, 1523. 10.1038/s41467-019-09234-6.

38. Chong, S.Z., Evrard, M., Devi, S., Chen, J., Lim, J.Y., See, P., Zhang, Y., Adrover, J.M., Lee, B., Tan, L., et al. (2016). CXCR4 identifies transitional bone marrow premonocytes that replenish the mature monocyte pool for peripheral responses. J Exp Med *213*, 2293–2314. 10.1084/jem.20160800.

39. Steppich, B., Dayyani, F., Gruber, R., Lorenz, R., Mack, M., and Ziegler-Heitbrock, H.W.L. (2000). Selective mobilization of CD14+CD16+ monocytes by exercise. Am. J. Physiol.-Cell Physiol. *279*, C578–C586. 10.1152/ajpcell.2000.279.3.c578.

40. Janssen, H., Kahles, F., Liu, D., Downey, J., Koekkoek, L.L., Roudko, V., D'Souza, D., McAlpine, C.S., Halle, L., Poller, W.C., et al. (2023). Monocytes re-enter the bone marrow during fasting and alter the host response to infection. Immunity *56*, 783-796.e7. 10.1016/j.immuni.2023.01.024.

41. Askenase, M.H., Han, S.-J., Byrd, A.L., Morais da Fonseca, D., Bouladoux, N., Wilhelm, C., Konkel, J.E., Hand, T.W., Lacerda-Queiroz, N., Su, X., et al. (2015). Bone-Marrow-Resident NK Cells Prime Monocytes for Regulatory Function during Infection. Immunity *42*, 1130–1142. 10.1016/j.immuni.2015.05.011.

42. Biram, A., Liu, J., Hezroni, H., Davidzohn, N., Schmiedel, D., Khatib-Massalha, E., Haddad, M., Grenov, A., Lebon, S., Salame, T.M., et al. (2022). Bacterial infection disrupts established germinal center reactions through monocyte recruitment and impaired metabolic adaptation. Immunity *55*, 442-458.e8. 10.1016/j.immuni.2022.01.013.

43. Papayannopoulos, V. (2018). Neutrophil extracellular traps in immunity and disease. Nat Rev Immunol *18*, 134–147. 10.1038/nri.2017.105.

44. Kolaczkowska, E., and Kubes, P. (2013). Neutrophil recruitment and function in health and inflammation. Nat. Rev. Immunol. *13*, 159–175. 10.1038/nri3399.

45. Castanheira, F.V.S., and Kubes, P. (2019). Neutrophils and NETs in modulating acute and chronic inflammation. Blood *133*, 2178–2185. 10.1182/blood-2018-11-844530.

46. Hartt, J.K., Barish, G., Murphy, P.M., and Gao, J.-L. (1999). N-Formylpeptides Induce Two Distinct Concentration Optima for Mouse Neutrophil Chemotaxis by Differential Interaction with Two N-Formylpeptide Receptor (Fpr) Subtypes. J Exp Medicine *190*, 741–748. 10.1084/jem.190.5.741.

47. Li, P., Li, M., Lindberg, M.R., Kennett, M.J., Xiong, N., and Wang, Y. (2010). PAD4 is essential for antibacterial innate immunity mediated by neutrophil extracellular traps. J Exp Med *207*, 1853–1862. 10.1084/jem.20100239.

48. Granger, V., Faille, D., Marani, V., Noël, B., Gallais, Y., Szely, N., Flament, H., Pallardy, M., Chollet-Martin, S., and Chaisemartin, L. (2017). Human blood monocytes are able to form extracellular traps. J. Leukoc. Biol. *102*, 775–781. 10.1189/jlb.3ma0916-411r.

49. Ginhoux, F., and Guilliams, M. (2016). Tissue-Resident Macrophage Ontogeny and Homeostasis. Immunity *44*, 439–449. 10.1016/j.immuni.2016.02.024.

50. Mildner, A., Yona, S., and Jung, S. (2013). Chapter Three A Close Encounter of the Third Kind Monocyte-Derived Cells. Adv. Immunol. *120*, 69–103. 10.1016/b978-0-12-417028-5.00003-x.

51. Varol, C., Vallon-Eberhard, A., Elinav, E., Aychek, T., Shapira, Y., Luche, H., Fehling, H.J., Hardt, W.-D., Shakhar, G., and Jung, S. (2009). Intestinal Lamina Propria Dendritic Cell Subsets Have Different Origin and Functions. Immunity *31*, 502–512. 10.1016/j.immuni.2009.06.025.

52. Diehl, G.E., Longman, R.S., Zhang, J.-X., Breart, B., Galan, C., Cuesta, A., Schwab, S.R., and Littman, D.R. (2013). Microbiota restricts trafficking of bacteria to mesenteric lymph nodes by CX3CR1hi cells. Nature *494*, 116–120. 10.1038/nature11809.

53. Aychek, T., Mildner, A., Yona, S., Kim, K.-W., Lampl, N., Reich-Zeliger, S., Boon, L., Yogev, N., Waisman, A., Cua, D.J., et al. (2015). IL-23-mediated mononuclear phagocyte crosstalk protects mice from Citrobacter rodentium-induced colon immunopathology. Nat. Commun. *6*, 6525. 10.1038/ncomms7525.

54. Bianchini, M., Duchêne, J., Santovito, D., Schloss, M.J., Evrard, M., Winkels, H., Aslani, M., Mohanta, S.K., Horckmans, M., Blanchet, X., et al. (2019). PD-L1 expression on nonclassical monocytes reveals their origin and immunoregulatory function. Sci Immunol *4*, eaar3054. 10.1126/sciimmunol.aar3054.

55. Gross-Vered, M., Trzebanski, S., Shemer, A., Bernshtein, B., Curato, C., Stelzer, G., Salame, T.-M., David, E., Boura-Halfon, S., Chappell-Maor, L., et al. (2020). Defining murine monocyte differentiation into colonic and ileal macrophages. Elife *9*, e49998. 10.7554/elife.49998.

56. Gibbings, S.L., Thomas, S.M., Atif, S.M., McCubbrey, A.L., Desch, A.N., Danhorn, T., Leach, S.M., Bratton, D.L., Henson, P.M., Janssen, W.J., et al. (2017). Three Unique Interstitial Macrophages in the Murine Lung at Steady State. Am. J. Respir. Cell Mol. Biology *57*, 66–76. 10.1165/rcmb.2016-0361oc.

57. Vanneste, D., Bai, Q., Hasan, S., Peng, W., Pirottin, D., Schyns, J., Maréchal, P., Ruscitti, C., Meunier, M., Liu, Z., et al. (2023). MafB-restricted local monocyte proliferation precedes lung interstitial macrophage differentiation. Nat. Immunol. *24*, 827–840. 10.1038/s41590-023-01468-3.

58. Chakarov, S., Lim, H.Y., Tan, L., Lim, S.Y., See, P., Lum, J., Zhang, X.-M., Foo, S., Nakamizo, S., Duan, K., et al. (2019). Two distinct interstitial macrophage populations coexist across tissues in specific subtissular niches. Science *363*, eaau0964. 10.1126/science.aau0964.

59. Goldmann, T., Wieghofer, P., Jordão, M.J.C., Prutek, F., Hagemeyer, N., Frenzel, K., Amann, L., Staszewski, O., Kierdorf, K., Krueger, M., et al. (2016). Origin, fate and dynamics

of macrophages at central nervous system interfaces. Nat Immunol *17*, 797–805. 10.1038/ni.3423.

60. Hove, H.V., Martens, L., Scheyltjens, I., Vlaminck, K.D., Antunes, A.R.P., Prijck, S.D., Vandamme, N., Schepper, S.D., Isterdael, G.V., Scott, C.L., et al. (2019). A single-cell atlas of mouse brain macrophages reveals unique transcriptional identities shaped by ontogeny and tissue environment. Nat. Neurosci. *22*, 1021–1035. 10.1038/s41593-019-0393-4.

61. Shemer, A., Grozovski, J., Tay, T.L., Tao, J., Volaski, A., Süß, P., Ardura-Fabregat, A., Gross-Vered, M., Kim, J.-S., David, E., et al. (2018). Engrafted parenchymal brain macrophages differ from microglia in transcriptome, chromatin landscape and response to challenge. Nat. Commun. *9*, 5206. 10.1038/s41467-018-07548-5.

62. Bain, C.C., Bravo-Blas, A., Scott, C.L., Perdiguero, E.G., Geissmann, F., Henri, S., Malissen, B., Osborne, L.C., Artis, D., and Mowat, A.M. (2014). Constant replenishment from circulating monocytes maintains the macrophage pool in the intestine of adult mice. Nat. Immunol. *15*, 929–937. 10.1038/ni.2967.

63. Cobo, I., Tanaka, T., Glass, C.K., and Yeang, C. (2022). Clonal hematopoiesis driven by DNMT3A and TET2 mutations: role in monocyte and macrophage biology and atherosclerotic cardiovascular disease. Curr. Opin. Hematol. *29*, 1–7. 10.1097/moh.0000000000000688.

64. Xie, Q., Klesney-Tait, J., Keck, K., Parlet, C., Borcherding, N., Kolb, R., Li, W., Tygrett, L., Waldschmidt, T., Olivier, A., et al. (2015). Characterization of a novel mouse model with genetic deletion of CD177. Protein Cell *6*, 117–126. 10.1007/s13238-014-0109-1.

65. Kamio, N., Yokota, A., Tokuda, Y., Ogasawara, C., Nakano, M., Nagao, M., Tashiro, K., Maekawa, T., Onai, N., and Hirai, H. (2021). A Novel CD135+ Subset of Mouse Monocytes with a Distinct Differentiation Pathway and Antigen-Presenting Properties. J Immunol Baltim Md 1950 *209*, 498–509. 10.4049/jimmunol.2100024.

66. Satoh, T., Nakagawa, K., Sugihara, F., Kuwahara, R., Ashihara, M., Yamane, F., Minowa, Y., Fukushima, K., Ebina, I., Yoshioka, Y., et al. (2017). Identification of an atypical monocyte and committed progenitor involved in fibrosis. Nature *541*, 96–101. 10.1038/nature20611.

67. Amorim, A., Feo, D.D., Friebel, E., Ingelfinger, F., Anderfuhren, C.D., Krishnarajah, S., Andreadou, M., Welsh, C.A., Liu, Z., Ginhoux, F., et al. (2022). IFNγ and GM-CSF control complementary differentiation programs in the monocyte-to-phagocyte transition during neuroinflammation. Nat. Immunol. *23*, 217–228. 10.1038/s41590-021-01117-7.

68. Giladi, A., Wagner, L.K., Li, H., Dörr, D., Medaglia, C., Paul, F., Shemer, A., Jung, S., Yona, S., Mack, M., et al. (2020). Cxcl10+ monocytes define a pathogenic subset in the central nervous system during autoimmune neuroinflammation. Nat. Immunol. *21*, 525–534. 10.1038/s41590-020-0661-1.

69. Goodridge, H.S. (2023). Aging of classical monocyte subsets. Aging (Albany NY) *15*, 290–292. 10.18632/aging.204493.

70. Barman, P.K., Shin, J.E., Lewis, S.A., Kang, S., Wu, D., Wang, Y., Yang, X., Nagarkatti, P.S., Nagarkatti, M., Messaoudi, I., et al. (2022). Production of MHCII-expressing classical

monocytes increases during aging in mice and humans. Aging Cell *21*, e13701. 10.1111/acel.13701.

71. Ikeda, N., Asano, K., Kikuchi, K., Uchida, Y., Ikegami, H., Takagi, R., Yotsumoto, S., Shibuya, T., Makino-Okamura, C., Fukuyama, H., et al. (2018). Emergence of immunoregulatory Ym1+Ly6Chi monocytes during recovery phase of tissue injury. Sci Immunol *3*, eaat0207. 10.1126/sciimmunol.aat0207.

72. Madisen, L., Zwingman, T.A., Sunkin, S.M., Oh, S.W., Zariwala, H.A., Gu, H., Ng, L.L., Palmiter, R.D., Hawrylycz, M.J., Jones, A.R., et al. (2010). A robust and high-throughput Cre reporting and characterization system for the whole mouse brain. Nat. Neurosci. *13*, 133–140. 10.1038/nn.2467.

73. Matsumoto, K., Mitani, T.T., Horiguchi, S.A., Kaneshiro, J., Murakami, T.C., Mano, T., Fujishima, H., Konno, A., Watanabe, T.M., Hirai, H., et al. (2019). Advanced CUBIC tissue clearing for whole-organ cell profiling. Nat. Protoc. *14*, 3506–3537. 10.1038/s41596-019-0240-9.

74. Scheyltjens, I., Hove, H.V., Vlaminck, K.D., Kancheva, D., Bastos, J., Vara-Pérez, M., Antunes, A.R.P., Martens, L., Scott, C.L., Ginderachter, J.A.V., et al. (2022). Single-cell RNA and protein profiling of immune cells from the mouse brain and its border tissues. Nat. Protoc. *17*, 2354–2388. 10.1038/s41596-022-00716-4.

75. Jaitin, D.A., Kenigsberg, E., Keren-Shaul, H., Elefant, N., Paul, F., Zaretsky, I., Mildner, A., Cohen, N., Jung, S., Tanay, A., et al. (2014). Massively Parallel Single-Cell RNA-Seq for Marker-Free Decomposition of Tissues into Cell Types. Science *343*, 776–779. 10.1126/science.1247651.

76. Kohen, R., Barlev, J., Hornung, G., Stelzer, G., Feldmesser, E., Kogan, K., Safran, M., and Leshkowitz, D. (2019). UTAP: User-friendly Transcriptome Analysis Pipeline. BMC Bioinform. *20*, 154. 10.1186/s12859-019-2728-2.

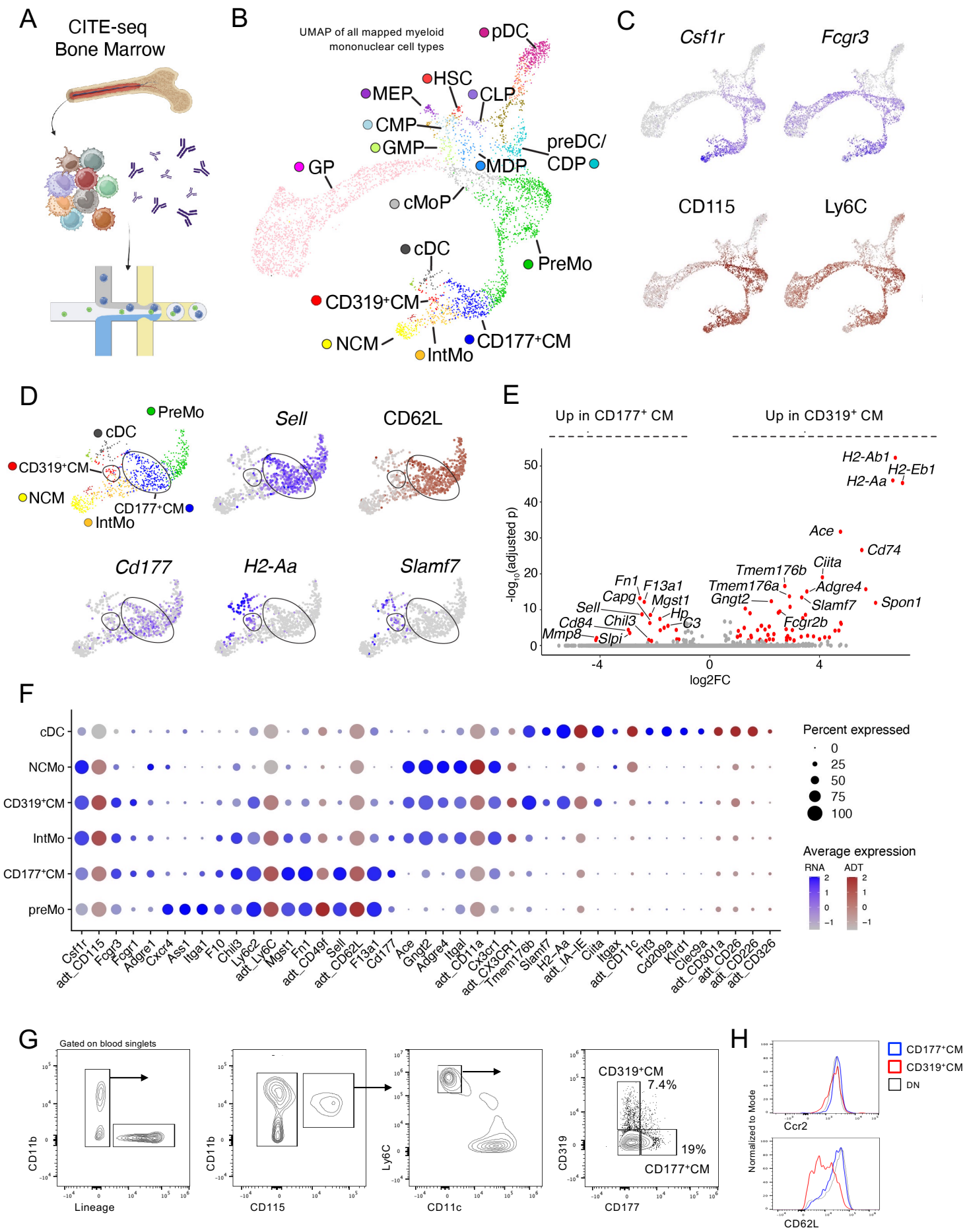
A
CITE-seq
Bone Marrow
B
UMAP of all mapped myeloid mononuclear cell types
pDC
HSC
MEP
CLP
CMP
GMP
preDC/CDP
MDP
GP
cMoP
cDC
PreMo
CD319+CM
NCM
IntMo
CD177+CM
C
Csf1r
Fcgr3
CD115
Ly6C
D
PreMo
cDC
CD319+CM
NCM
CD177+CM
IntMo
Sell
CD62L
Cd177
H2-Aa
Slamf7
E
Up in CD177+ CM
Up in CD319+ CM
-log10(adjusted p)
log2FC
H2-Ab1
H2-Eb1
H2-Aa
Ace
Cd74
Ciita
Tmem176b
Tmem176a
Adgre4
Gngt2
Slamf7
Spon1
Fcgr2b
Fn1
F13a1
Capg
Mgst1
Sell
Hp
C3
Cd84
Chil3
Mmp8
Slpi
F
cDC
NCMo
CD319+CM
IntMo
CD177+CM
preMo
Csf1r
adt_CD115
Fcgr3
Fcgr1
Adgre1
Cxcr4
Ass1
Itga1
F10
Chil3
Ly6c2
adt_Ly6C
Mgst1
Fn1
adt_CD49f
Sell
adt_CD62L
F13a1
Cd177
Ace
Gngt2
Adgre4
Itgal
adt_CD11a
Cx3cr1
adt_CX3CR1
Tmem176b
Slamf7
H2--Aa
adt_IA-IE
Ciita
Itgax
adt_CD11c
Flt3
Cd209a
Klrd1
Clec9a
adt_CD301a
adt_CD26
adt_CD226
adt_CD326
Percent expressed
0
25
50
75
100
Average expression
RNA
ADT
G
Gated on blood singlets
CD11b
Lineage
CD115
Ly6C
CD11c
CD319+CM
7.4%
19%
CD177+CM
CD319
CD177
H
CD177+CM
CD319+CM
DN
Normalized to Mode
Ccr2
CD62L

Figure 1

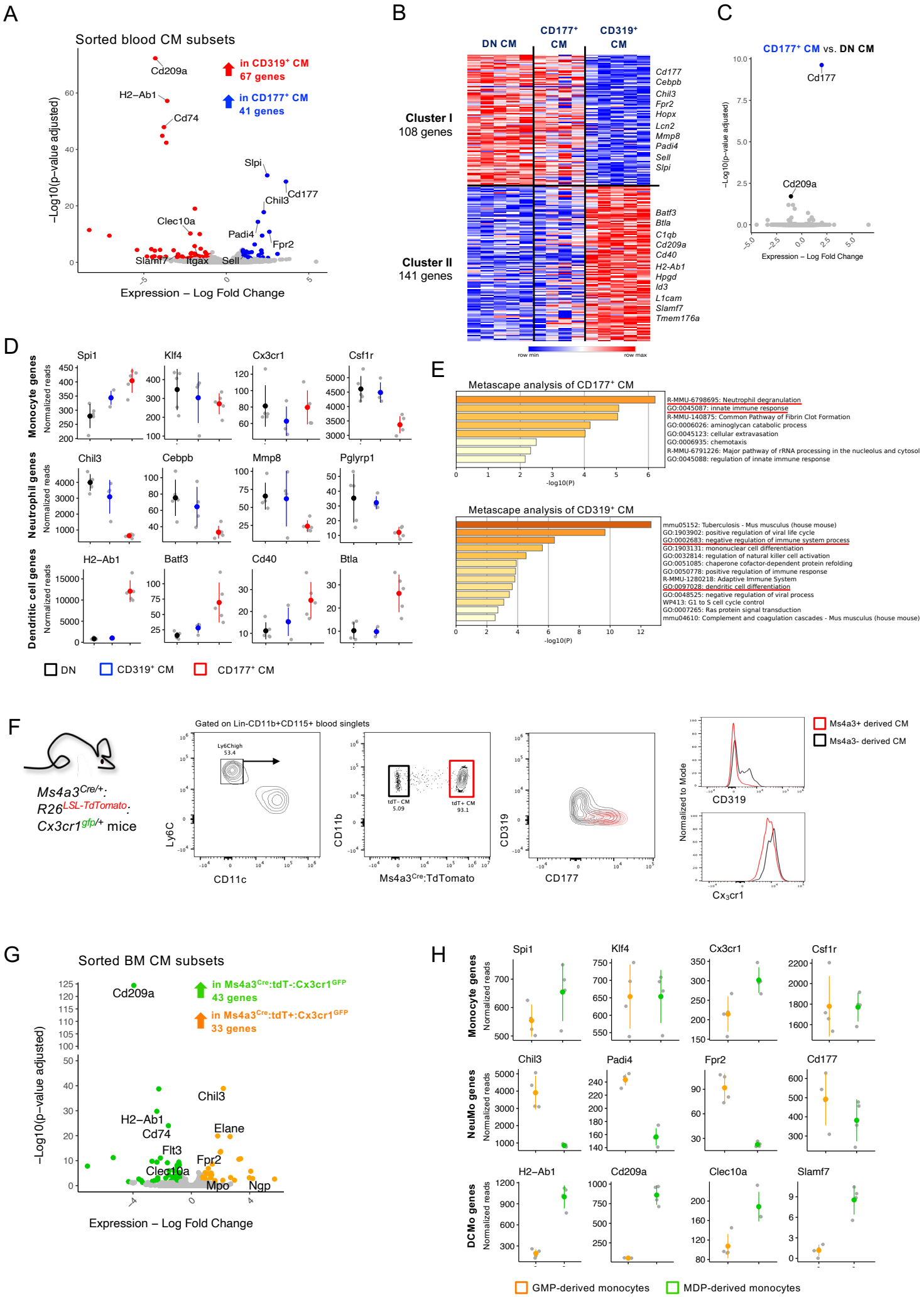
A
Sorted blood CM subsets
in CD319+ CM
67 genes
in CD177+ CM
41 genes
Cd209a
H2–Ab1
Cd74
Slpi
Cd177
Chil3
Clec10a
Padi4
Fpr2
Slamf7
Itgax
Sell
–Log10(p–value adjusted)
Expression – Log Fold Change
B
DN CM
CD177+ CM
CD319+ CM
Cluster I
108 genes
Cluster II
141 genes
Cd177
Cebpb
Chil3
Fpr2
Hopx
Lcn2
Mmp8
Padi4
Sell
Slpi
Batf3
Btla
C1qb
Cd209a
Cd40
H2-Ab1
Hpgd
Id3
L1cam
Slamf7
Tmem176a
row min
row max
C
CD177+ CM vs. DN CM
Cd177
Cd209a
–Log10(p–value adjusted)
Expression – Log Fold Change
D
Monocyte genes
Neutrophil genes
Dendritic cell genes
Normalized reads
Spi1
Klf4
Cx3cr1
Csf1r
Chil3
Cebpb
Mmp8
Pglyrp1
H2–Ab1
Batf3
Cd40
Btla
DN
CD319+ CM
CD177+ CM
E
Metascape analysis of CD177+ CM
R-MMU-6798695: Neutrophil degranulation
GO:0045087: innate immune response
R-MMU-140875: Common Pathway of Fibrin Clot Formation
GO:0006026: aminoglycan catabolic process
GO:0045123: cellular extravasation
GO:0006935: chemotaxis
R-MMU-6791226: Major pathway of rRNA processing in the nucleolus and cytosol
GO:0045088: regulation of innate immune response
-log10(P)
Metascape analysis of CD319+ CM
mmu05152: Tuberculosis - Mus musculus (house mouse)
GO:1903902: positive regulation of viral life cycle
GO:0002683: negative regulation of immune system process
GO:1903131: mononuclear cell differentiation
GO:0032814: regulation of natural killer cell activation
GO:0051085: chaperone cofactor-dependent protein refolding
GO:0050778: positive regulation of immune response
R-MMU-1280218: Adaptive Immune System
GO:0097028: dendritic cell differentiation
GO:0048525: negative regulation of viral process
WP413: G1 to S cell cycle control
GO:0007265: Ras protein signal transduction
mmu04610: Complement and coagulation cascades - Mus musculus (house mouse)
-log10(P)
F
Ms4a3Cre/+:
R26LSL-TdTomato:
Cx3cr1gfp/+ mice
Gated on Lin-CD11b+CD115+ blood singlets
Ly6Chigh
53.4
Ly6C
CD11c
tdT- CM
5.09
tdT+ CM
93.1
CD11b
Ms4a3Cre:TdTomato
CD319
CD177
Ms4a3+ derived CM
Ms4a3- derived CM
Normalized to Mode
CD319
Cx3cr1
G
Sorted BM CM subsets
in Ms4a3Cre:tdT-:Cx3cr1GFP
43 genes
in Ms4a3Cre:tdT+:Cx3cr1GFP
33 genes
Cd209a
Chil3
H2–Ab1
Cd74
Elane
Flt3
Fpr2
Clec10a
Mpo
Ngp
–Log10(p–value adjusted)
Expression – Log Fold Change
H
Monocyte genes
NeuMo genes
DCMo genes
Normalized reads
Spi1
Klf4
Cx3cr1
Csf1r
Chil3
Padi4
Fpr2
Cd177
H2–Ab1
Cd209a
Clec10a
Slamf7
GMP-derived monocytes
MDP-derived monocytes

Figure 2

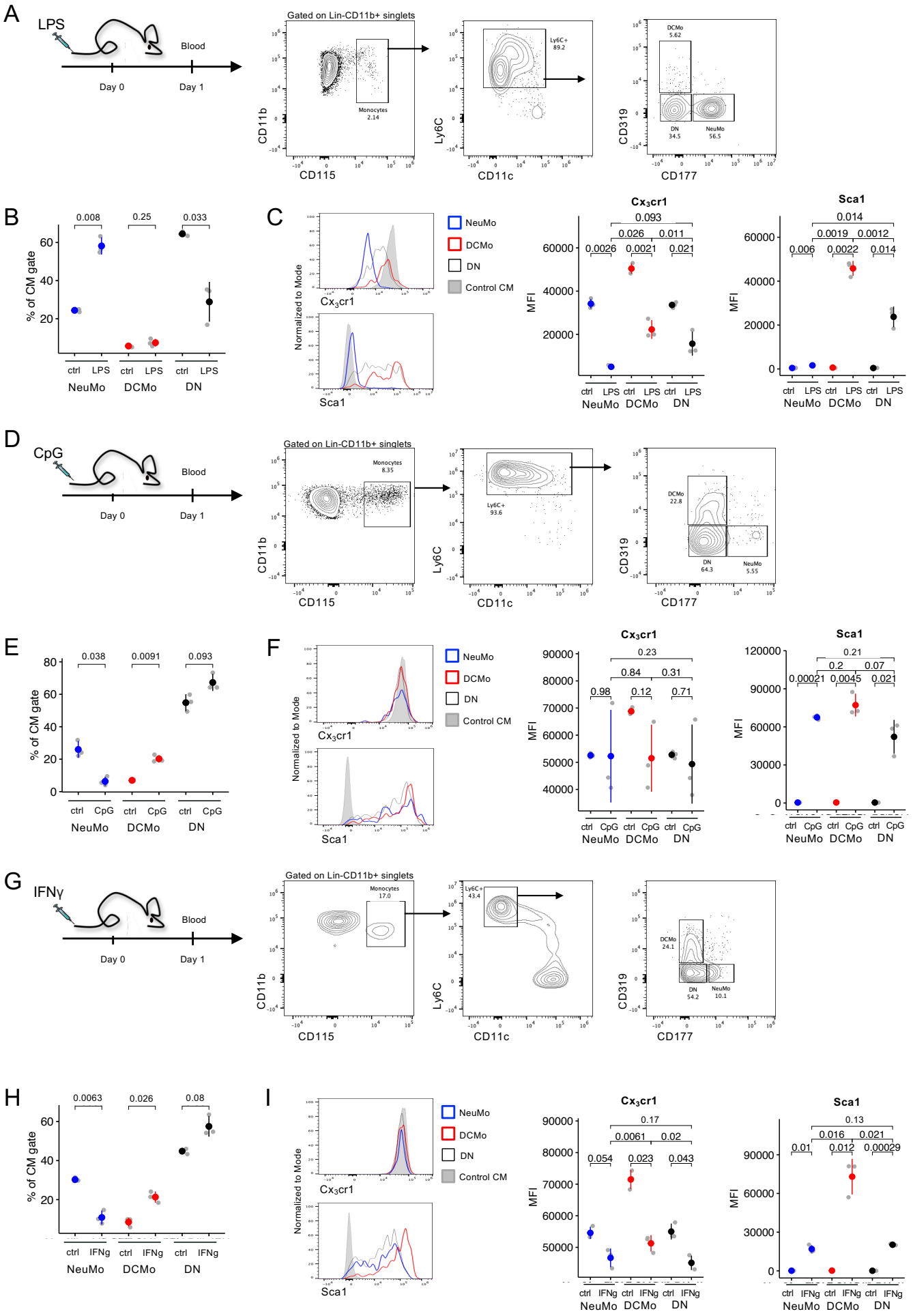
A
LPS
Blood
Day 0
Day 1
Gated on Lin-CD11b+ singlets
Monocytes 2.14
CD11b
CD115
Ly6C+ 89.2
Ly6C
CD11c
DCMo 5.62
DN 34.5
NeuMo 56.5
CD319
CD177
B
% of CM gate
0.008
0.25
0.033
ctrl LPS ctrl LPS ctrl LPS
NeuMo DCMo DN
C
Normalized to Mode
Cx3cr1
Sca1
NeuMo
DCMo
DN
Control CM
MFI
0.093
0.026 0.011
0.0026 0.0021 0.021
0.014
0.0019 0.0012
0.006 0.0022 0.014
D
CpG
Monocytes 8.35
Ly6C+ 93.6
DCMo 22.8
DN 64.3
NeuMo 5.55
E
0.038
0.0091
0.093
ctrl CpG ctrl CpG ctrl CpG
F
0.23
0.84 0.31
0.98 0.12 0.71
0.21
0.2 0.07
0.00021 0.0045 0.021
G
IFNγ
Monocytes 17.0
Ly6C+ 43.4
DCMo 24.1
DN 54.2
NeuMo 10.1
H
0.0063
0.026
0.08
ctrl IFNg ctrl IFNg ctrl IFNg
I
0.17
0.0061 0.02
0.054 0.023 0.043
0.13
0.016 0.021
0.01 0.012 0.00029

Figure 3

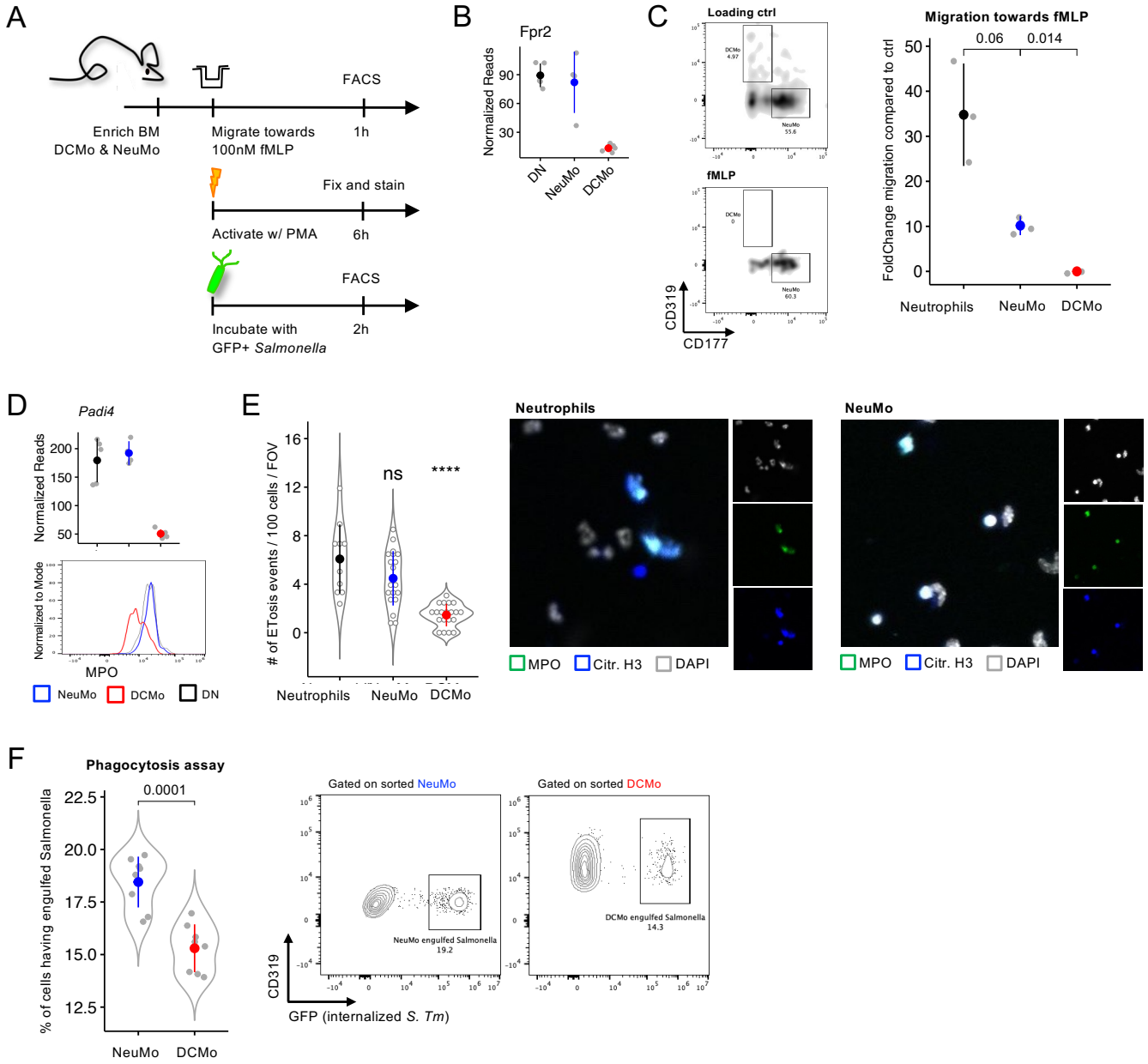
A
FACS
Enrich BM
DCMo & NeuMo
Migrate towards
100nM fMLP
1h
Fix and stain
Activate w/ PMA
6h
FACS
Incubate with
GFP+ Salmonella
2h
B
Fpr2
Normalized Reads
DN
NeuMo
DCMo
C
Loading ctrl
fMLP
CD319
CD177
Migration towards fMLP
0.06
0.014
FoldChange migration compared to ctrl
Neutrophils
NeuMo
DCMo
D
Padi4
Normalized Reads
Normalized to Mode
MPO
NeuMo
DCMo
DN
E
# of ETosis events / 100 cells / FOV
ns
****
Neutrophils
NeuMo
DCMo
Neutrophils
NeuMo
MPO
Citr. H3
DAPI
F
Phagocytosis assay
0.0001
% of cells having engulfed Salmonella
NeuMo
DCMo
Gated on sorted NeuMo
Gated on sorted DCMo
NeuMo engulfed Salmonella
19.2
DCMo engulfed Salmonella
14.3
CD319
GFP (internalized S. Tm)

Figure 4

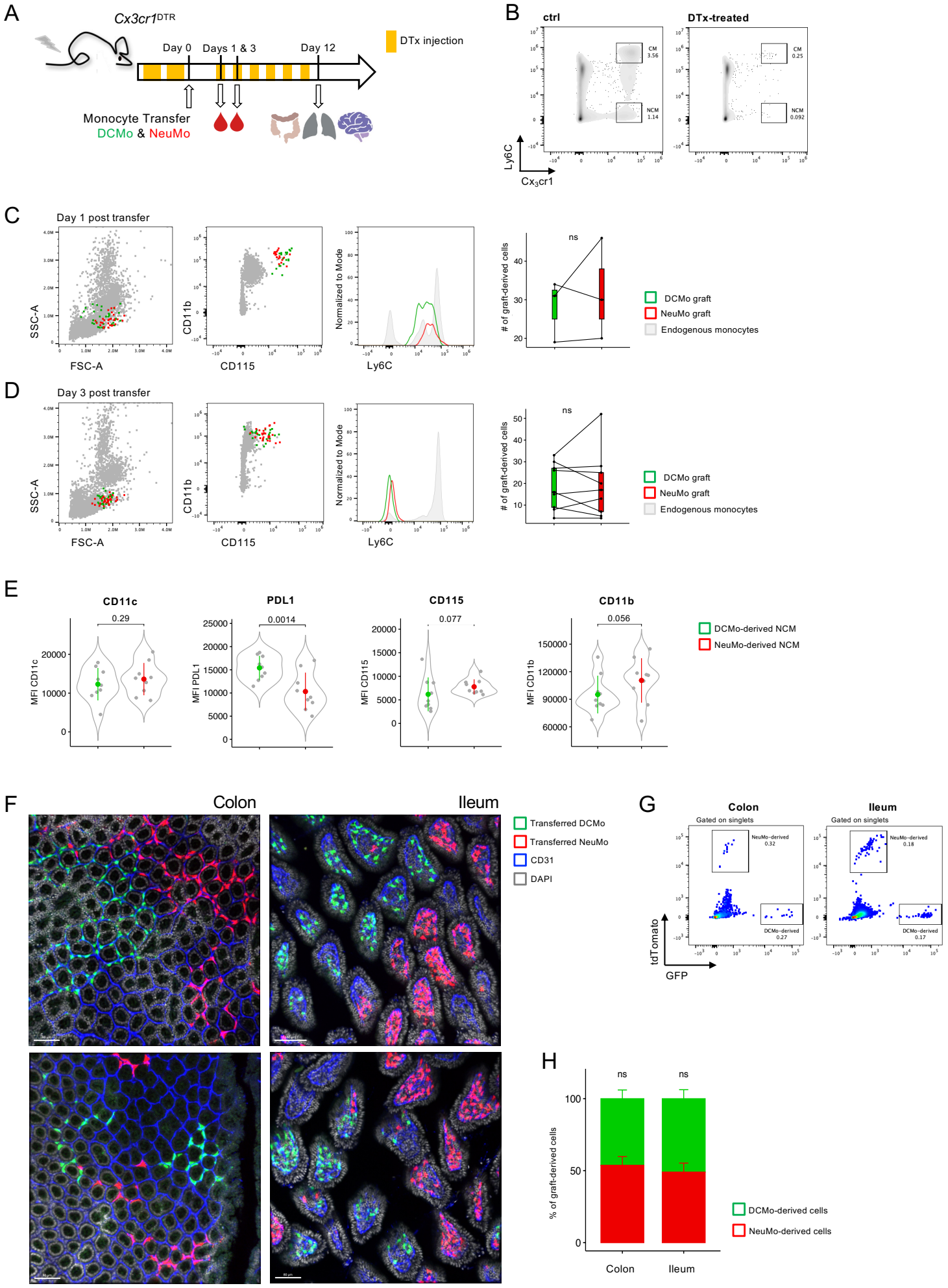
A
Cx3cr1DTR
Day 0
Days 1 & 3
Day 12
DTx injection
Monocyte Transfer
DCMo & NeuMo
B
ctrl
DTx-treated
CM 3.56
NCM 1.14
CM 0.25
NCM 0.092
Ly6C
Cx3cr1
C
Day 1 post transfer
SSC-A
FSC-A
CD11b
CD115
Normalized to Mode
Ly6C
# of graft-derived cells
ns
DCMo graft
NeuMo graft
Endogenous monocytes
D
Day 3 post transfer
SSC-A
FSC-A
CD11b
CD115
Normalized to Mode
Ly6C
# of graft-derived cells
ns
DCMo graft
NeuMo graft
Endogenous monocytes
E
CD11c
0.29
MFI CD11c
PDL1
0.0014
MFI PDL1
CD115
0.077
MFI CD115
CD11b
0.056
MFI CD11b
DCMo-derived NCM
NeuMo-derived NCM
F
Colon
Ileum
Transferred DCMo
Transferred NeuMo
CD31
DAPI
G
Colon
Ileum
Gated on singlets
NeuMo-derived 0.32
DCMo-derived 0.27
NeuMo-derived 0.18
DCMo-derived 0.17
tdTomato
GFP
H
ns
ns
% of graft-derived cells
DCMo-derived cells
NeuMo-derived cells
Colon
Ileum

Figure 5

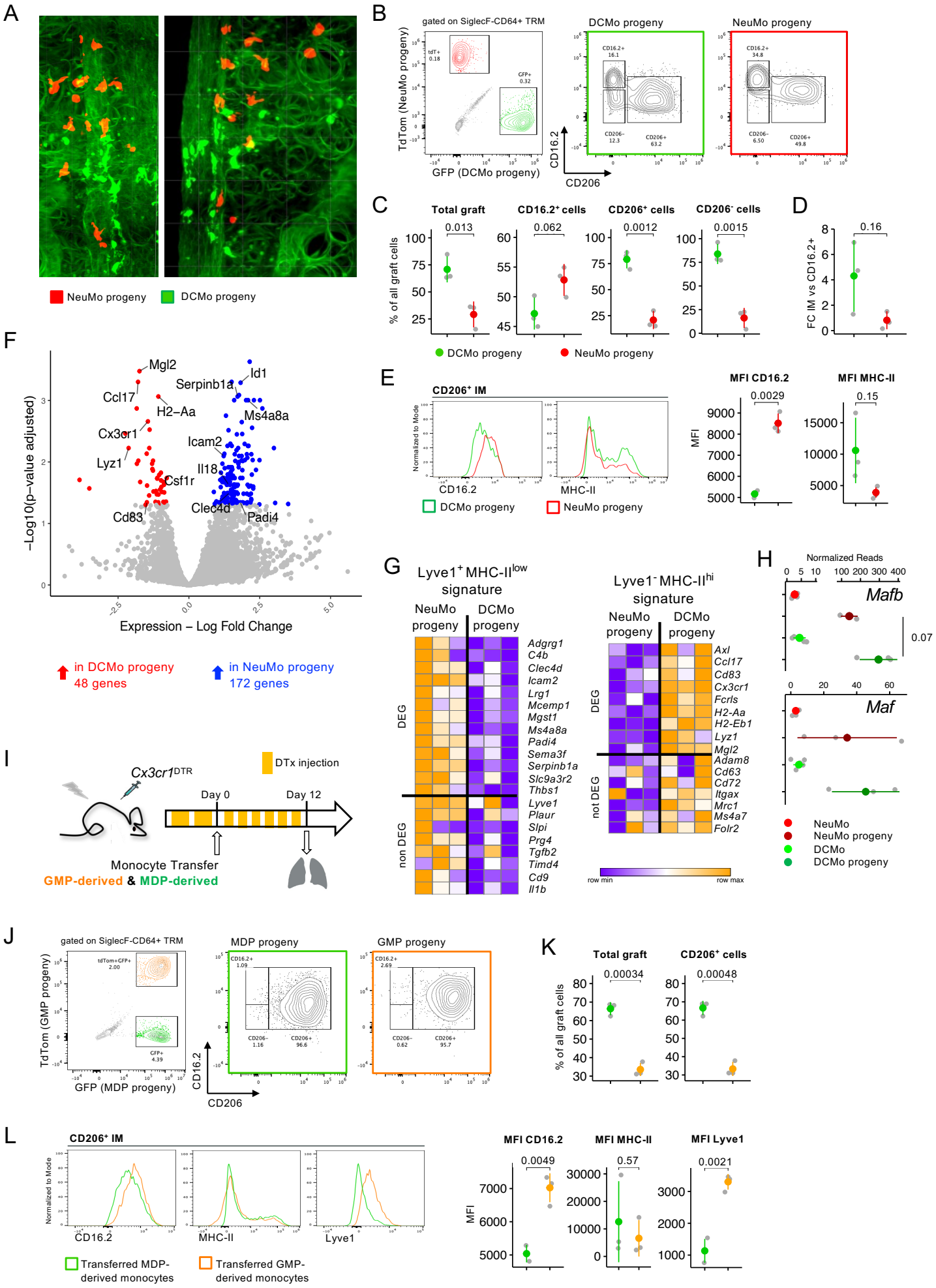
A
NeuMo progeny
DCMo progeny
B
gated on SiglecF-CD64+ TRM
TdTom (NeuMo progeny)
GFP (DCMo progeny)
DCMo progeny
NeuMo progeny
CD16.2
CD206
C
Total graft
CD16.2+ cells
CD206+ cells
CD206- cells
% of all graft cells
0.013
0.062
0.0012
0.0015
DCMo progeny
NeuMo progeny
D
FC IM vs CD16.2+
0.16
E
CD206+ IM
Normalized to Mode
CD16.2
MHC-II
DCMo progeny
NeuMo progeny
MFI CD16.2
MFI MHC-II
MFI
0.0029
0.15
F
-Log10(p-value adjusted)
Expression – Log Fold Change
Mgl2
Ccl17
H2-Aa
Cx3cr1
Lyz1
Csf1r
Cd83
Id1
Serpinb1a
Ms4a8a
Icam2
Il18
Clec4d
Padi4
in DCMo progeny
48 genes
in NeuMo progeny
172 genes
G
Lyve1+ MHC-IIlow signature
Lyve1- MHC-IIhi signature
NeuMo progeny
DCMo progeny
DEG
non DEG
not DEG
Adgrg1
C4b
Clec4d
Icam2
Lrg1
Mcemp1
Mgst1
Ms4a8a
Padi4
Sema3f
Serpinb1a
Slc9a3r2
Thbs1
Lyve1
Plaur
Slpi
Prg4
Tgfb2
Timd4
Cd9
Il1b
Axl
Ccl17
Cd83
Cx3cr1
Fcrls
H2-Aa
H2-Eb1
Lyz1
Mgl2
Adam8
Cd63
Cd72
Itgax
Mrc1
Ms4a7
Folr2
row min
row max
H
Normalized Reads
Mafb
Maf
0.07
NeuMo
NeuMo progeny
DCMo
DCMo progeny
I
Cx3cr1DTR
DTx injection
Day 0
Day 12
Monocyte Transfer
GMP-derived & MDP-derived
J
gated on SiglecF-CD64+ TRM
TdTom (GMP progeny)
GFP (MDP progeny)
MDP progeny
GMP progeny
CD16.2
CD206
K
Total graft
CD206+ cells
% of all graft cells
0.00034
0.00048
L
CD206+ IM
Normalized to Mode
CD16.2
MHC-II
Lyve1
Transferred MDP-derived monocytes
Transferred GMP-derived monocytes
MFI CD16.2
MFI MHC-II
MFI Lyve1
MFI
0.0049
0.57
0.0021

Figure 6

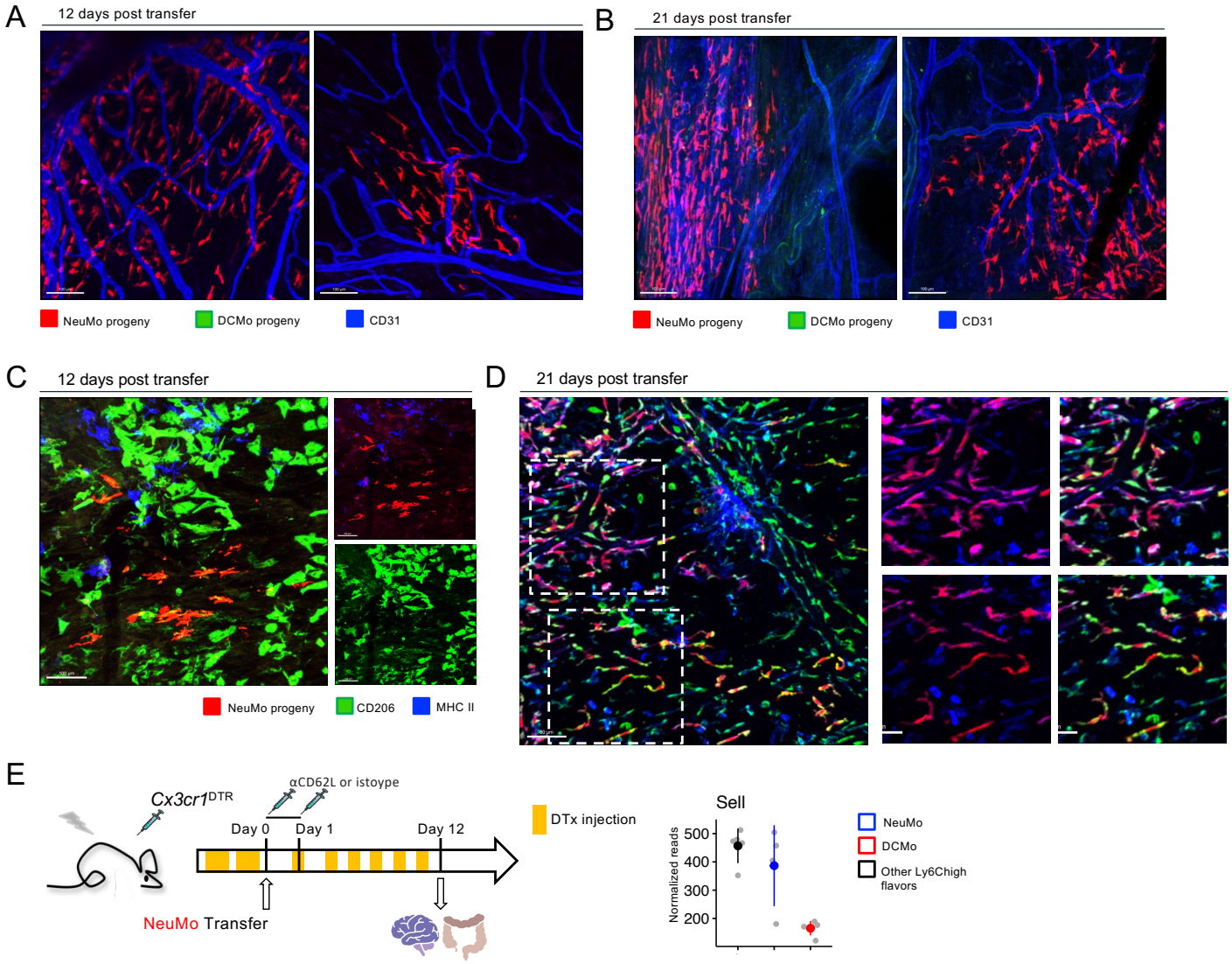
A
12 days post transfer
NeuMo progeny
DCMo progeny
CD31
B
21 days post transfer
NeuMo progeny
DCMo progeny
CD31
C
12 days post transfer
NeuMo progeny
CD206
MHC II
D
21 days post transfer
E
Cx3cr1DTR
αCD62L or istoype
Day 0
Day 1
Day 12
DTx injection
NeuMo Transfer
Sell
Normalized reads
500
400
300
200
NeuMo
DCMo
Other Ly6Chigh flavors

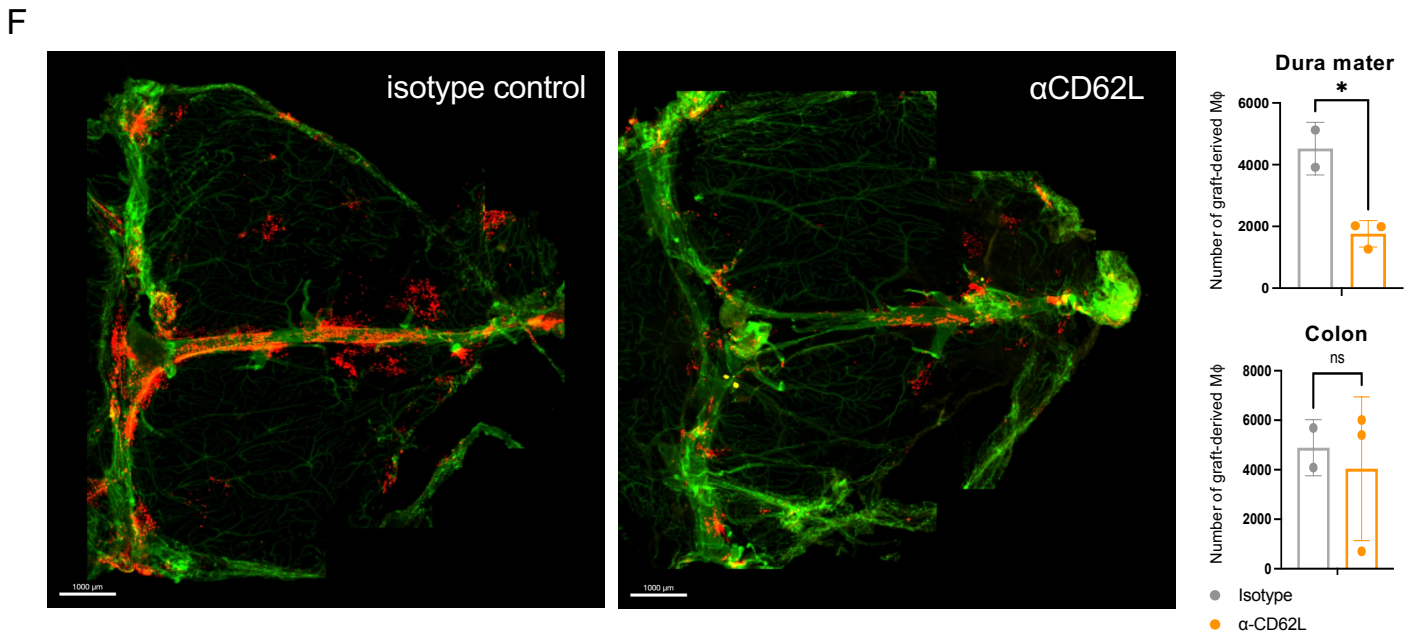
F
isotype control
αCD62L
1000 µm
Dura mater
*
Number of graft-derived Mϕ
6000
4000
2000
0
Colon
ns
8000
6000
4000
2000
0
Isotype
α-CD62L

Figure 7

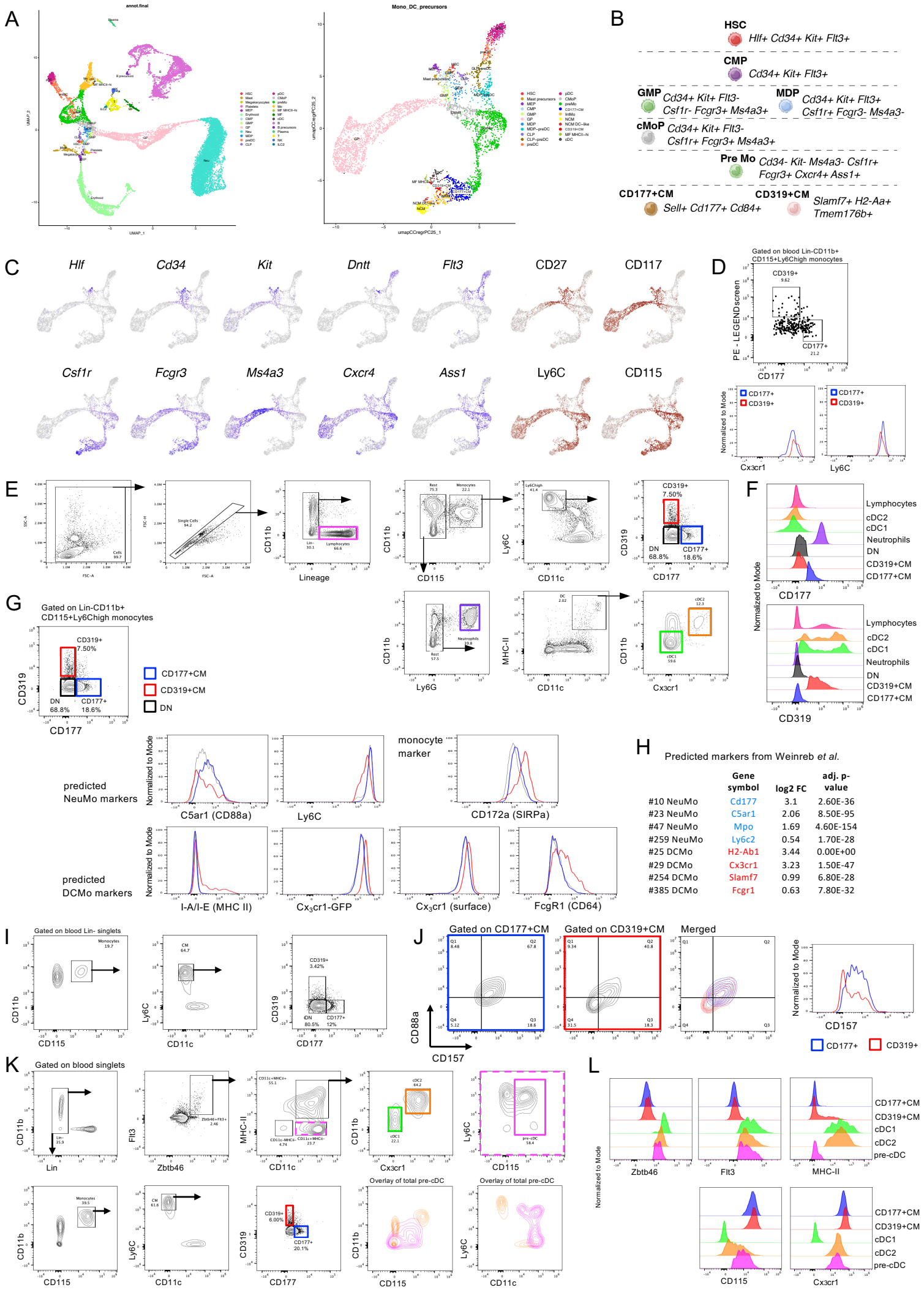

Suppl Figure 1

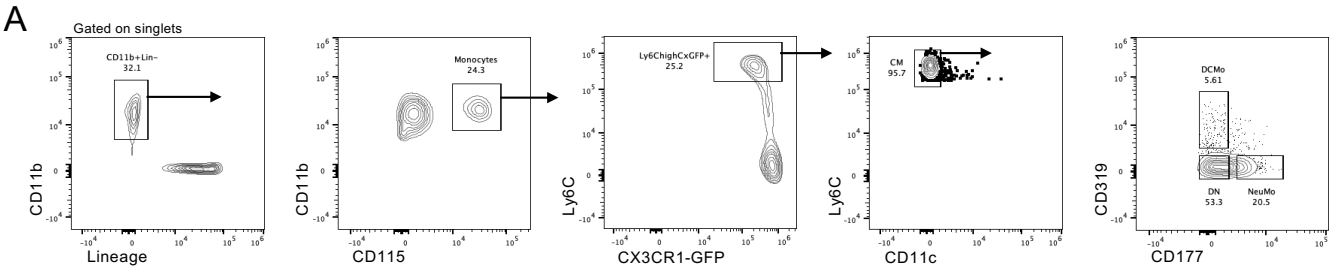

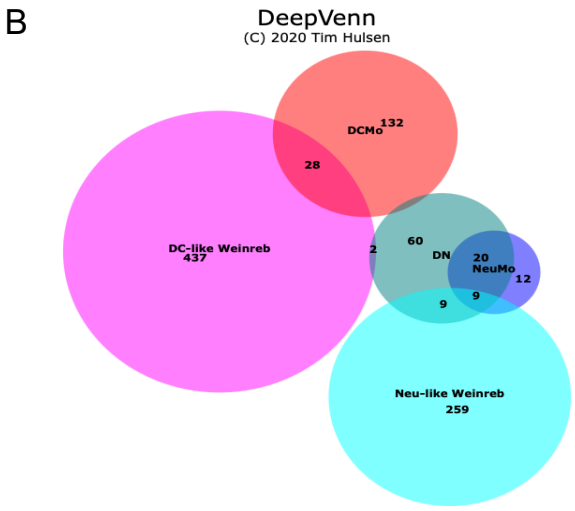

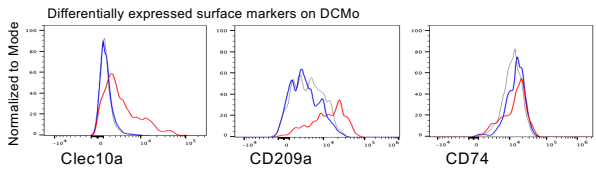

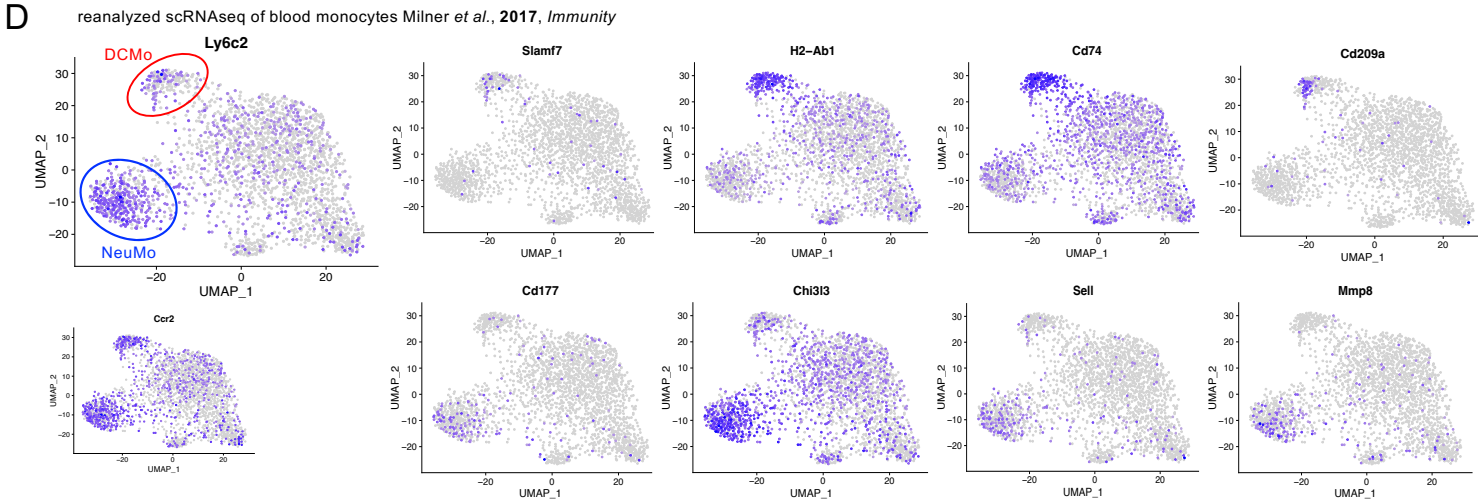

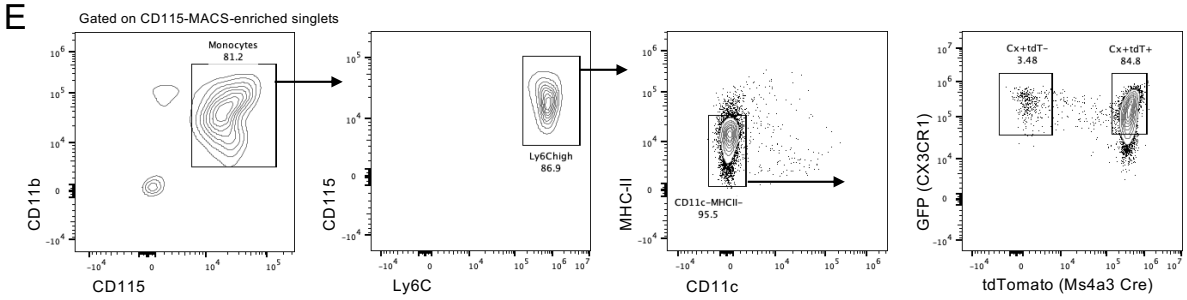

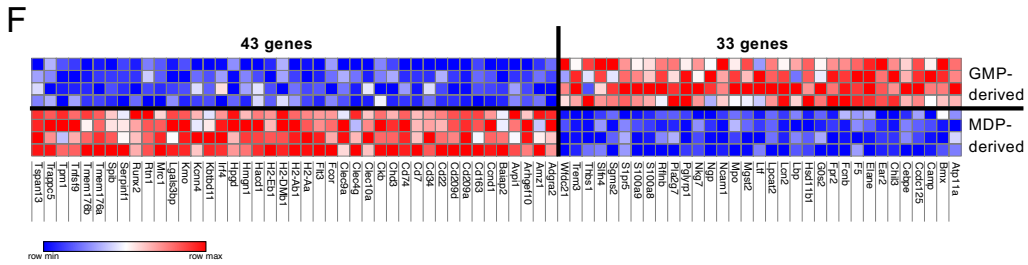

Suppl Figure 2

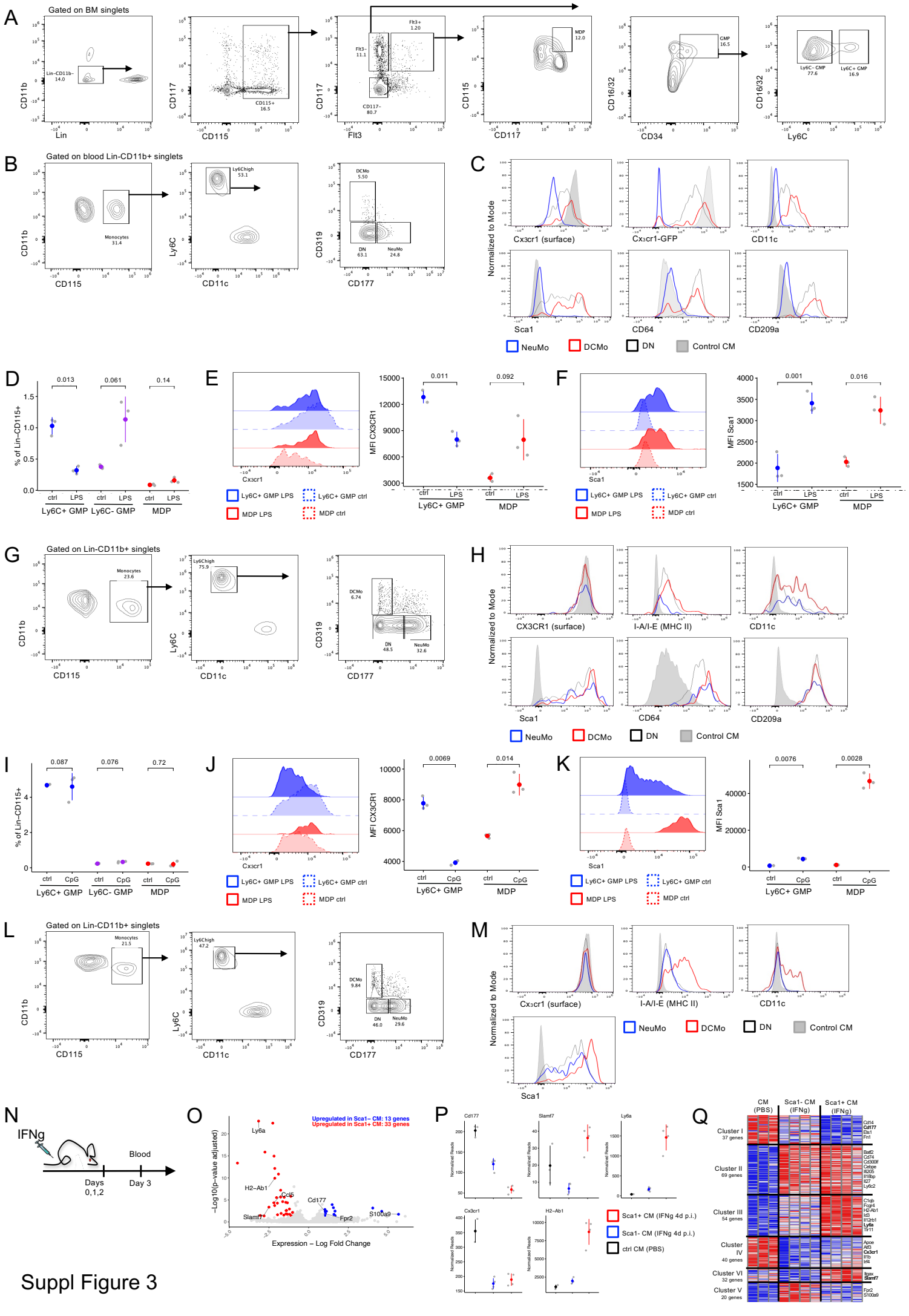

Suppl Figure 3

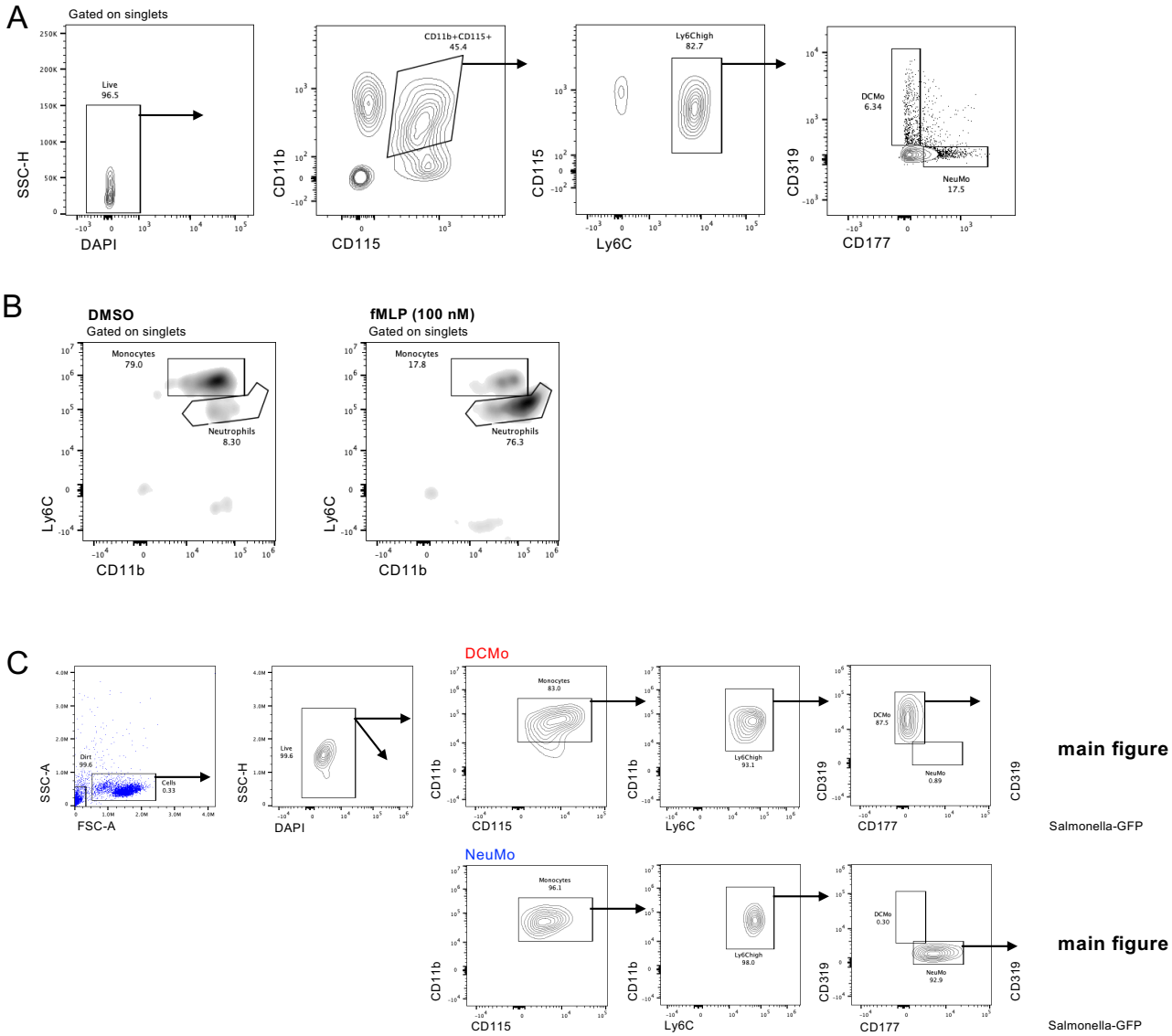

Suppl Figure 4

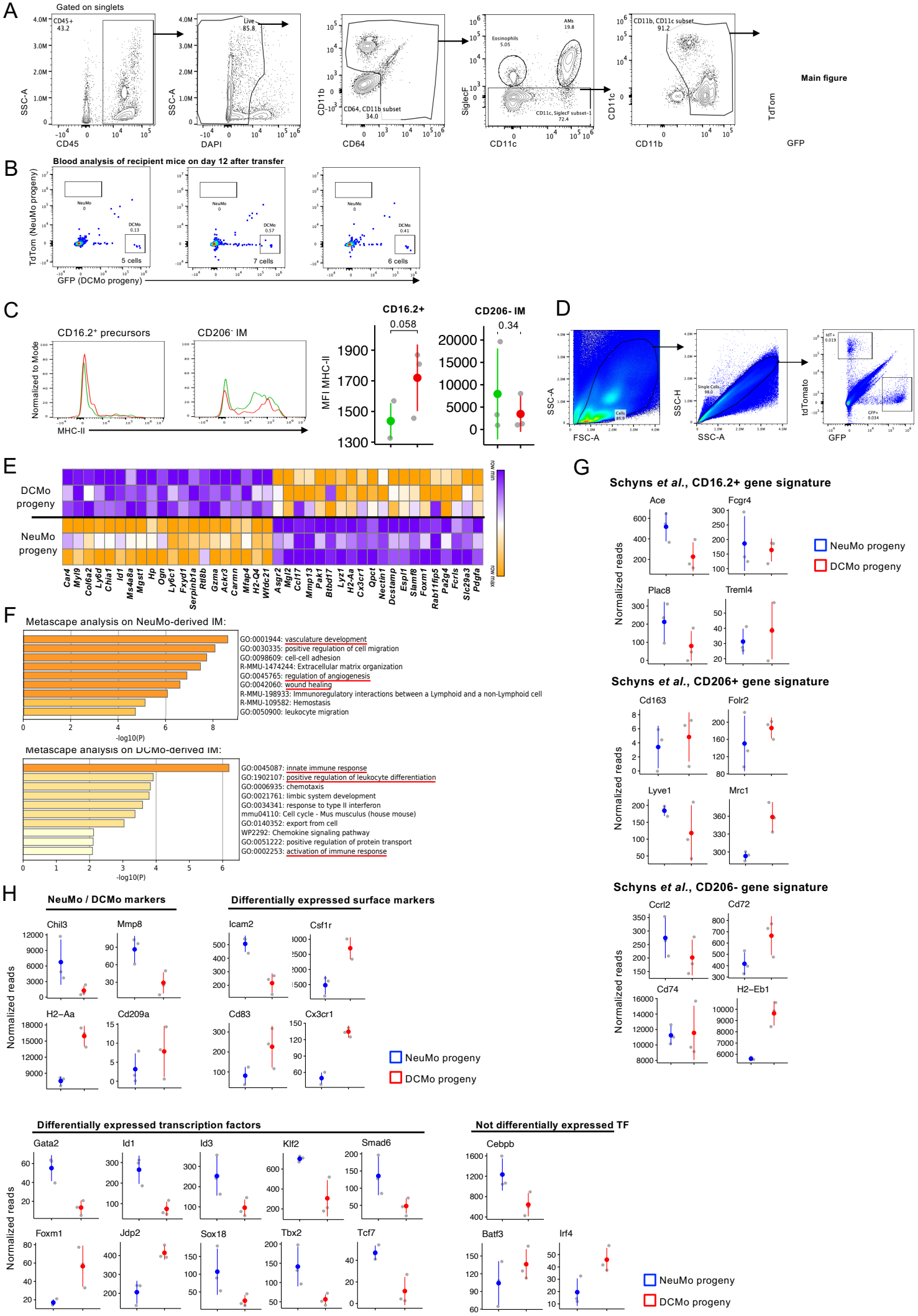

Suppl Figure 5

A Parenchyma, 21 days post transfer

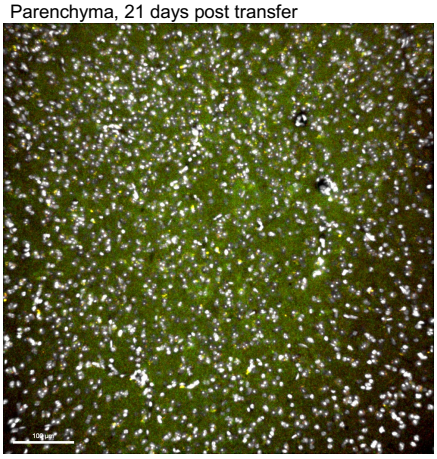

Transferred NeuMo Transferred DCMo DAPI

B Leptomeninges, 12 days post transfer

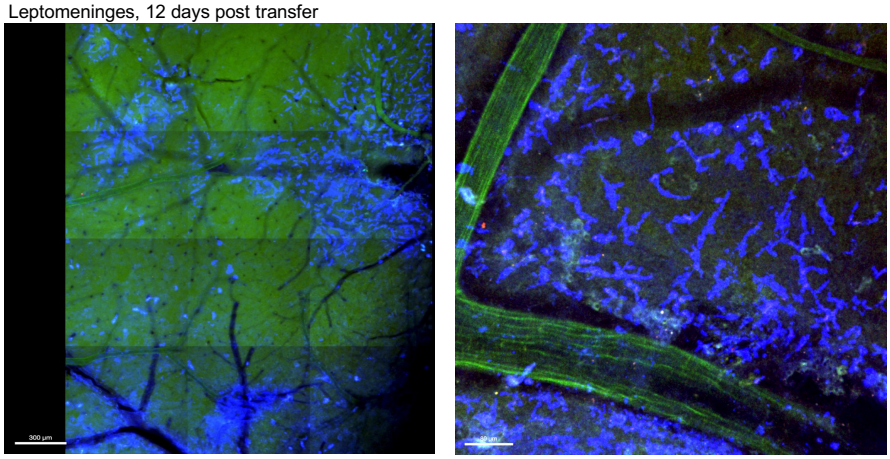

Transferred NeuMo Transferred DCMo CD206

C Dura mater, 12 days post transfer

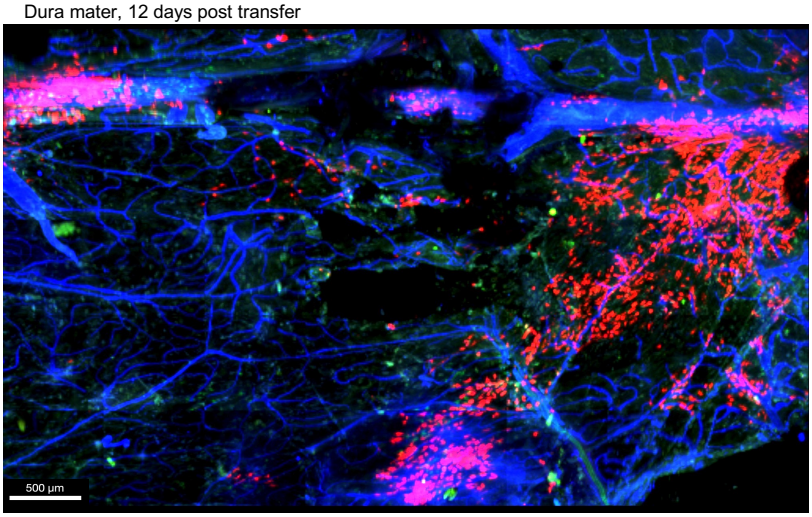

D Sagittal sinus & periphery

Periphery

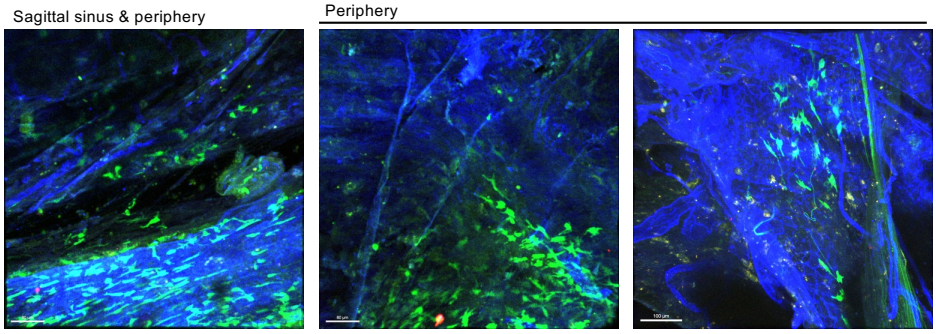

Transferred Cx3cr1-GFP NeuMo Transferred Cx3cr1-Cre:tdTomato DCMo CD31

E Colon, isotype control

Colon, αCD62L

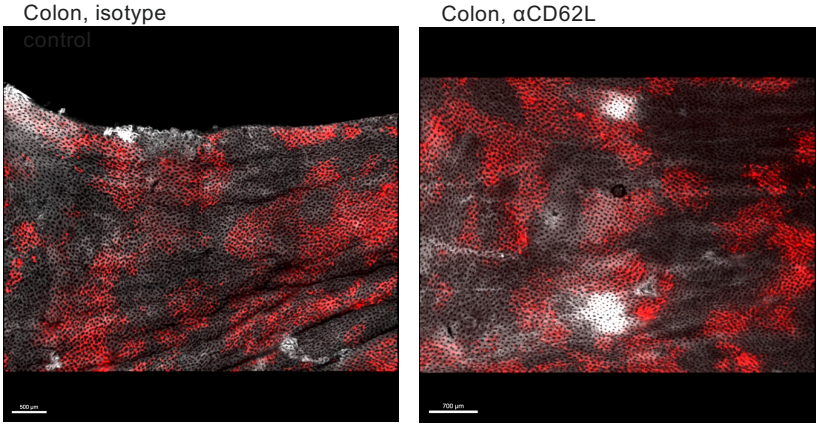

Suppl Figure 6